



January 2020

Experimental Acquisition Of An Endwall Heat Distribution In A Linear Turbine Cascade

Maliha Yel Mahi

Follow this and additional works at: <https://commons.und.edu/theses>

Recommended Citation

Yel Mahi, Maliha, "Experimental Acquisition Of An Endwall Heat Distribution In A Linear Turbine Cascade" (2020). *Theses and Dissertations*. 3396.
<https://commons.und.edu/theses/3396>

This Thesis is brought to you for free and open access by the Theses, Dissertations, and Senior Projects at UND Scholarly Commons. It has been accepted for inclusion in Theses and Dissertations by an authorized administrator of UND Scholarly Commons. For more information, please contact und.common@library.und.edu.

**EXPERIMENTAL ACQUISITION OF AN ENDWALL HEAT
DISTRIBUTION IN A LINEAR TURBINE CASCADE**

By

Maliha Yel Mahi

Bachelor of Science, Bangladesh University of Professionals, 2014

A Thesis

Submitted to the Graduate Faculty

Of the

University of North Dakota

in partial fulfillment of the requirements

for the degree of

Master of Science

Grand Forks, North Dakota

December
2020

This thesis submitted by Maliha Yel Mahi in partial fulfillment of the requirements for the degree of Master of Science from the University of North Dakota, has been read by the Faculty Advisory Committee under whom the work has been done and hereby approved.

Dr. Forrest Ames

Date

Dr. Clement Tang

Date

Dr. Anjali Sandip

Date

This thesis is being submitted by the Appointed advisory committee as having met all the requirements of the School of Graduate Studies at the University of North Dakota and is hereby approved.

Chris Nelson
Dean of the School of Graduate Studies

Date

PERMISSION

Title	EXPERIMENTAL ACQUISITION OF AN ENDWALL HEAT DISTRIBUTION IN A LINEAR TURBINE CASCADE
Department	Mechanical Engineering
Degree	Master of Science

In presenting this thesis in partial fulfillment of the requirements for a graduate degree from the University of North Dakota, I agree that the library of the University shall make it freely available for inspection. I further agree that the permission for extensive copying for scholarly purposes may be granted by the professor who supervised my thesis work or, in his absence, by the Chairperson of the department or the dean of the School of Graduate Studies. It is understood that any copying or publication or other use of this thesis or part thereof for financial gain shall not be allowed without my written permission. It is also understood that due recognition shall be given to me and to the University of North Dakota in any scholarly use which may be made of any material in my thesis.

Maliha Yel Mahi
December 2020

ACKNOWLEDGEMENT

I wish to express my sincere appreciation to my Advisory Committee members for their guidance and support during my time in the master's program at the University of North Dakota.

To my Mom and Dad, The world's best parents!

Table of Contents

ABSTRACT	xiii
CHAPTER I	1
INTRODUCTION	1
CHAPTER II	3
LITERARY REVIEW	3
Secondary Flows.....	3
Endwall heat transfer	5
Infrared Thermography for Temperature Measurement.....	8
CHAPTER III	11
EXPERIMENTAL APPROACH	11
Filter Box.....	12
Blower	13
Diffusers	14
Heat Exchanger.....	14
Flow Mixer	16
Straightener.....	17
Screen Box.....	17
Turbulence Generators	18

Low Turbulence Nozzle	18
Mock Aeroderivative Combustor	22
High Turbulence Nozzle.....	23
Cascade Test Section.....	24
Bleed Flow Adjustments	25
Exit Tailboards	27
IR Camera Mounting System	27
Camera mount.....	28
IR Window and Window Holder.....	29
Installation	30
Turbine Vanes.....	32
Pressure Vane	32
Heat Transfer Vane.....	34
The Endwall.....	35
Exit Diffuser	40
Oblique Diffuser	41
Pressure Measurements	42
The Data Acquisition System.....	43
Power Supply.....	43
Temperature Measurements	43

Procedure	45
Image Processing	47
CHAPTER IV	54
EXPERIMENTAL RESULTS.....	54
Uncertainty Analysis	54
Inlet and Exit Pressure Distributions	57
Vane Pressure Distribution	59
Endwall Heat Transfer Measurements	61
Endwall Stanton Number Distributions.....	63
CHAPTER V	94
CONCLUSION	94
APPENDIX A	97
CASCADE DIMENSIONS	97
APPENDIX B.....	102
CAMERA MOUNT DIMENSION.....	102
APPENDIX C	103
UNCERTAINTY ANALYSIS OF STANTON NUMBERS	103
REFERENCES.....	104

LIST OF FIGURES

Figure 1 Endwall flow model by Langston et al. [2]	9
Figure 2 Endwall vortex model of Wang, Olson, Goldstein, and Eckert [4].....	10
Figure 3 Large scale low-velocity wind tunnel.....	12
Figure 4 New York Blower used for Wind Tunnel	13
Figure 5 Schematic of wind tunnel heat exchanger	15
Figure 6 Flow mixer.....	16
Figure 7 Flow straightener	17
Figure 8 Screen box	18
Figure 9 Low turbulence nozzle	19
Figure 10 Small grid far configuration (left) and Small grid near configuration (right)	20
Figure 11 Large grid configuration.....	21
Figure 12 Mock aero-derivative configuration	22
Figure 13 High turbulence nozzle configuration	23
Figure 14 Layout of Cascade	25
Figure 15 Lower tailboard (left) and upper tailboard (right)	26
Figure 16 Therm app camera	28
Figure 17 Camera mount	29
Figure 18 The window holder and zinc selenide window	30
Figure 19 Experimental setup of the IR Cameras	31
Figure 20 Pressure vane	33
Figure 21 Heat transfer vane wrapped in Inconel foil	34
Figure 22 Cascade near endwall	36

Figure 23 Cascade far endwall.....	38
Figure 24 painted enwall surface	39
Figure 25 The exit diffuser	40
Figure 26 The oblique diffuser	41
Figure 27 Power supply	42
Figure 28 Data acquisition tower.....	44
Figure 29 Location of the thermocouples along the endwall surface	48
Figure 30 Web Interface and workspace of the “WebPlotDigitizer” GUI	53
Figure 31 Estimation of the Offset for each Camera (camera 1 through camera 5).....	56
Figure 32 Low turbulence inlet pressure distribution Re 1,000,000.....	58
Figure 33 Low turbulence exit pressure distribution Re 1,000,000.....	59
Figure 34 Low turbulence vane pressure distribution Re 1,000,000	61
Figure 35 Endwall Stanton number distributions for low turbulence condition, $Tu = 0.007$, $Re_C = 500,000$	65
Figure 36 Endwall Stanton number distributions for small grid far turbulence condition, $Tu = 0.035$, $Re_C = 500,000$	67
Figure 37 Endwall Stanton number distributions for large grid turbulence condition, $Tu = 0.081$, $Re_C = 500,000$	69
Figure 38 Endwall Stanton number distributions for aero derivative condition, $Tu = 0.137$, $Re_C = 500,000$	71
Figure 39 Endwall Stanton number distributions for high turbulence condition, $Tu = 0.174$, $Re_C = 500,000$	73

Figure 40 Endwall Stanton number distributions for low turbulence condition, $Tu = 0.007$, $Re_C = 1,000,000$	75
Figure 41 Endwall Stanton number distributions for small grid far turbulence condition, $Tu = 0.035$, $Re_C = 1,000,000$	77
Figure 42 Endwall Stanton number distributions for large grid turbulence condition, $Tu = 0.081$, $Re_C = 1,000,000$	79
Figure 43 Endwall Stanton number distributions for aero-derivative turbulence condition, $Tu = 0.137$, $Re_C = 1,000,000$	81
Figure 44 Endwall Stanton number distributions for high turbulence condition, $Tu = 0.174$, $Re_C = 1,000,000$	83
Figure 45 Endwall Stanton number distributions for low turbulence condition, $Tu = 0.007$, $Re_C = 2,000,000$	85
Figure 46 Endwall Stanton number distributions for small grid far turbulence condition, $Tu = 0.035$, $Re_C = 2,000,000$	87
Figure 47 Endwall Stanton number distributions for large grid turbulence condition, $Tu = 0.081$, $Re_C = 2,000,000$	89
Figure 48 Endwall Stanton number distributions for aero-derivative turbulence condition, $Tu = 0.137$, $Re_C = 2,000,000$	91
Figure 49 Endwall Stanton number distributions for high turbulence condition, $Tu = 0.174$, $Re_C = 2,000,000$	93
Figure 50 Cascade far endwall dimensions	97
Figure 51 Cascade near endwall dimensions.....	98
Figure 52 Cascade bottom dimensions	99

Figure 53 Cascade top dimensions	99
Figure 54 Cascade front dimensions.....	100
Figure 55 Cascade back dimensions.....	100
Figure 56 Vane dimensions	101

LIST OF TABLES

Table 1 Camera and Thermocouple information	49
Table 2 Camera ID and Corresponding Estimated Offset	56

ABSTRACT

The focus of this research is the experimental acquisition of endwall heat transfer distributions for an aft loaded vane with a large leading edge. This study will investigate endwall heat transfer distributions over five inlet turbulence levels ranging from intensities of 0.7% through very high turbulence levels as high as 17.4%. The investigation will be conducted at three varying Reynolds numbers based on true chord length and exit conditions ranging from 500,000 to 2000,000. The infrared thermography technique will be applied to the acquisition of the endwall heat transfer data due to the full surface image which can be developed from the acquired thermographs. An in situ calibration technique will be used to enhance the measurement accuracy. The experiment was conducted in a linear cascade test section, consisting of four turbine vanes with upper and lower bleed flows. Linear Cascade can reflect most of the flow characteristics in real gas turbine nozzles. This experiment exhibits some other advantages, such as geometric simplicity, simple adjustment, and large blade sections. This study will emphasize the effect of turbulence and Reynolds number on endwall heat transfer to ease cooling systems development for both turbine vanes and endwalls. Two different measurements were taken, one with the endwall heated and the other with the endwall heat turned off to ground the in situ calibration. The surface heat transfer was taken at three varying based on exit Reynolds number and was exhibited in terms of Stanton number based on exit conditions.

It is expected that the low turbulence heat transfer contours exhibit strong evidence of the impact

of secondary flows on heat transfer patterns as influenced by the vane's leading edge region and the pressure surface to the suction surface pressure gradient. Heat transfer contours at higher turbulence levels are expected to show weaker secondary flow evidence due to the enhanced turbulent mixing and flow instability. However, the higher turbulence levels are expected to generate higher levels of heat transfer near the leading edge and downstream from the wake, and in the passage due to earlier transition. These measurements are expected to provide benchmark quality data to ground the development of high-fidelity predictive tools.

CHAPTER I

INTRODUCTION

Gas turbine engines have become an integral part of our daily lives through the propulsion of aircraft, tanks, and large naval ships and by providing power to the electric grid. Turbine entry temperatures are continuously increasing to achieve a higher power output or thermal efficiency, to the extent that it significantly exceeds the allowable temperature for turbine component materials. Consequently, due to the urgency for continual improvement, the competitive market place is pushing the industry to introduce more efficient and durable engine designs while maintaining low NO_x combustion systems on par with stringent emission requirements. However, the real challenge is to develop more effective methods to cool and protect turbine components, especially the endwall of the first stage guide vane. Accurately predicting the cooling performance of endwall plays a crucial role in the development of cooling methods, which reliably extend a component's life span.

Even though it is challenging to measure heat fluxes on the components of gas turbines, it is crucial to predict accurately local heat loads under real engine representative conditions to ensure the credibility of designs. One of the primary purposes of the turbine designer is to develop a practical scheme to optimize the overall engine efficiency. A comprehensive database of endwall heat transfer distributions are primarily needed to help ground predictive methods.

This study investigated the experimental acquisition of endwall heat transfer distribution across a range of relevant turbulent conditions, accessible to designers with pertinent endwall heat

transfer information. The experiment was conducted in a linear vane cascade consisted of four aft loaded turbine vanes with a large leading edge. The larger leading edge helps to reduce the heat load of leading-edge and stagnation region by reducing the rate of streamwise acceleration. [1].

Infrared thermography technique is applied in this study to provide us a better understanding of heat transfer distribution of the whole endwall surface, which is achieved by stitching thermographs of the different locations to get the entire surface image. An in situ calibration technique is also applied for the measurement accuracy. For in situ calibration, around 47 thermocouples are installed at known locations of the endwall surface. Any discrepancies between thermography calibration and thermocouple calibration are taken into account for accuracy.

CHAPTER II

LITERARY REVIEW

Unfortunately for many years, the engineering attention has been emphasized on improving cooling design methods for turbine vanes and blades. However, the focus has been diverted into developing a sophisticated cooling scheme for the endwall in response to the endwall cooling problem.

Secondary Flows

Secondary flows are known as one of the most commonplace troublesome three-dimensional flow. These secondary flows cause aerodynamic losses and can significantly affect the heat transfer distribution of endwall. Although many researchers have examined secondary flows, a three-dimensional model developed by Langston, Nice, and Hooper [2] is widely accepted and has been verified by several studies. In their work, they used a large scale, low aspect ratio linear cascade of four turbine vanes. This model, presented in Figure 1, shows that horseshoe vortex forms upstream of the vane leading edge and the pressure surface leg is pushed towards the suction surface while the suction surface leg wraps around the suction surface and is pushed up off the endwall and onto the surface by passage vortex. The pressure leg is drawn up into the cascade passage vortex, where it is mixed with the passage pressure to suction endwall flow to form the passage vortex. The suction leg is drawn into the adjacent passage, rotates in the opposite direction of the passage vortex.

This leg is named as the counter vortex rotates about the axis of the passage vortex; it can be compared to a planet revolving around the sun. Sharma and Butler [3] have observed a similar pattern of secondary flows with the difference that the suction-side horseshoe vortex begins to wrap around the passage vortex. A thorough investigation of secondary flow near the endwall has been done by Wang et al. [4]. This experiment has been done by tracing multiple tracks of smoke wire which have been visualized within a laser light sheet. They provided the most elaborate explanation of the multi-vortex secondary flow patterns, as shown in Figure 2.

Further work is necessary to validate the inferred modification through the application of flow field measurements of pressure, velocities, and vorticities. Recently Ingram et al. [5] discovered a novel secondary flow feature while investigating in a turbine cascade with endwall profiling. They found a three-dimensional feature stemming from the strong convex/concave curvature in the early part of the passage near the suction surface.

Research on secondary flows has not been restricted to gain visualization of these flow patterns; they also focused their research on acquiring the effects of secondary flow on endwall heat transfer and determining their influence on aerodynamic losses. Ames et al. [5] investigated the impact of turbulent conditions (low & high) on secondary flows. They found low turbulence experienced robust secondary flow vectors and could be seen at specific regions of the endwall surface where secondary losses have impact on heat transfer of the endwall. Many researchers have investigated different approaches to mitigate the aerodynamic and secondary losses due to secondary vortices. N.H.K Chowdhury [6] found that a contracting inlet cascade with an aft loaded vane profile shows a significant reduction in losses at the low turbulent condition. This phenomenon can be attributed to the development of secondary flows for the contracting inlet cascade. Zess and Thole [7] focused their investigation on the influence of fillet radii on the

reduction of secondary losses. Their result shows a reduced turbulent kinetic energy level, which is a significant contributor to aerodynamic losses in an vane passage, was reduced at all locations in the endwall region (up to nearly 80 %) by reducing the unsteady horseshoe vortex. A similar kind of result has been exhibited by Sebastian et al. [8], who investigated the effect of fillet on secondary loss. Besides, they found no trace of corner vortices during the flow visualization at the trailing edge. Recently, D. C. Knezevici et al. [9] found that endwall contouring is a useful source of reducing endwall losses by developing a weaker passage vortex. The experiment was performed at an inlet Reynolds number of 126,000 based on inlet midspan velocity and axial chord.

Endwall heat transfer

Endwalls in turbines experience a very high gas temperature, which can overcome the cooling scheme of the endwall. So, understandably, the primary requirement to inhibit endwall cooling failure is to develop a better knowledge of the heat transfer distribution of the turbine endwall. In the process of researching endwall heat transfer distributions, many researchers have investigated the endwall heat transfer load by using different methodologies and experimental apparatuses. York et al. [10] investigated the endwall heat transfer in a linear vane cascade to examine the effects of exit Mach number, exit Reynolds number, inlet boundary layer thickness, gas-to-wall temperature ratio, inlet pressure gradients, and inlet temperature gradients. The finite element method was used to solve for the local surface heat flux based on the relative temperature and location of hot and cold side thermocouples. They acquired endwall adiabatic temperature contours, endwall heated temperature contours, and determined endwall local Stanton number contours. They found evidence of the effects of the horseshoe vortex in the curvature of the isotherms around the suction surface leading edge and in the penetration of the isotherms into the

passage entrance region. Heat transfer of the non-adiabatic endwall showed a pattern of isotherms which curve around the pressure surface leading edge. Giel et al. [11] investigated turbine blade endwall heat transfer measurements varying Reynolds and Mach numbers. The steady-state liquid crystal technique was applied to obtain Endwall heat transfer data. Heat transfer measurements were made at two Reynolds numbers and each of two exit Mach numbers with a low turbulence inlet condition and a high level of turbulence. High Stanton number levels are seen very close to the blade, near its stagnation point. As the flow accelerates around the suction surface, there is a region of very high heat transfer. The data show the significant differences in the heat transfer distributions that resulted from variations in Reynolds number, exit Mach number, and inlet turbulence grid. For each of the cases, however, a peak heat transfer region occurred in a small downstream region, between 3 to 6 diameters downstream of the trailing edge. But surprisingly, they found that the turbulence grid made the peak Stanton number lower than that of no turbulence grid. Goldstein and Spores [12] used a naphthalene sublimation mass transfer technique to acquire detailed distributions of the local endwall transport coefficient. Contours of the heat transfer Stanton number were derived from the local endwall transport coefficients. Their results showed an increased heat transfer region at the leading edge of the blade and blade wake region. Ames et al. [13] investigated endwall heat transfer distributions for varying turbulence conditions and for different Reynolds numbers. The experiment was performed using thermochromic liquid crystal thermometry. They found the overall influence of turbulence on endwall heat transfer was less dramatic for the higher Reynolds number cases. The high turbulence heat transfer contours show weaker evidence of the impact of secondary flows on heat transfer patterns due to the enhanced turbulent mixing and because the larger scales tend to push around the flow structures. In contrast, the low turbulence

heat transfer contours show strong evidence of the impact of secondary flows on heat transfer patterns. Arisi et al. [14] conducted extensive research on the endwall heat transfer characteristics on a nozzle platform that has been misaligned with the combustor exit, resulting in a backward-facing step at the nozzle inlet. They found passage vortex and horseshoe vortex dominates the heat transfer of flat endwall while the passage vortex and horseshoe vortex become weakened in the presence of a configuration with an upstream step. They also observed that the upstream step configuration experienced a strong lateral gradient in heat transfer downstream of the throat. In contrast, heat transfer is fairly uniform downstream of the throat for a flat configuration. Zhigang LI et al. [15] investigated the effects of upstream step geometry on the endwall secondary flow and heat transfer in a transonic linear turbine vane passage with axisymmetric converging endwalls. However, unlike the backward-facing upstream step geometry, the forward-facing upstream geometry minimized the high thermal load region. It reduced the heat transfer coefficient, especially for the suction side regions near the vane leading edge. T. W. Simon et al. [16] thoroughly reviewed the effect of different factors on endwall heat transfer. After analyzing various research, they concluded that secondary flow has a strong effect on the heat transfer rate on endwalls. The heat transfer rate on endwalls depended not only on secondary flows, but they also found the effect of turbulence, Mach number, surface roughness can be counted for the heat transfer rate on the endwall. They also discussed heat transfer in both blown cascades and blown contoured cascades. Alan Thrift et al. [17] investigated the heat transfer distribution of a nozzle guide vane endwall by varying the combustor-turbine slot orientation to 90 deg, 65 deg, 45 deg, and 30 deg. They experimented by utilizing leakage flow from the combustor-turbine interface as a coolant at two different leakage coolant momentum flux ratios: a real momentum flux ratio and a low momentum flux ratio. Their research indicates

that injecting coolant at the engine real momentum flux ratio reduced the net heat flux (as high as 137% at 45 deg slot orientation) to the endwall at each point within the vane passage for all four slot orientations. Even though reducing the interface slot orientation for low momentum injection improved the net heat flux reduction; still, the highest area average is comparatively lower than that of higher momentum injection. G. Barigozzi et al. [18] analyzed heat transfer measurement with film cooling varying different tangential positions of a generic inlet flow nonuniformity generated by a blunt body located upstream of a high-pressure NGV cascade. They employed the transient ThermoChromic Liquid Crystal technique to measure the heat transfer coefficient, which is later verified by Heat Flux Microsensors. They found inlet flow nonuniformity has an impact on the endwall heat transfer depending on the relative position of the blunt-body and the aerofoil. Aligning the inflow nonuniformity with the vane leading edge increases the heat flux in the vane passage. In contrast, a reduction in the heat flux is observed if inlet flow distortion is moved toward the suction sides of the adjacent vane. Recently Xing Yang et al. [19] experimentally studied heat transfer characteristics over high-pressure turbine endwall surfaces with film cooling. The experiment was performed based on the superposition principle using a steady high-resolution IR technique. They found Reynolds number has a significant effect over the endwall surface. There is an improvement of the overall heat transfer level in the endwall surface with increasing Reynolds number.

Infrared Thermography for Temperature Measurement

Among the vast applications of infrared thermography, investigating the heat transfer distribution of endwall by achieving temperature data from thermography is promising. Infrared thermography (IRT) is a science subjected to the acquisition and processing of thermal information from IR cameras. Infrared radiation emitted by an object can be obtained by Infrared

measuring devices and transformed into an electronic signal. As the Infrared technique is a non-intrusive technique, there is no disturbance in the temperature field. Applying the infrared method for temperature measurement has become popular among researchers. Recently, Varty et al. [1] used IR camera pictures to examine the suction surface of the vane when it was heated and unheated. They observed [1] the influence of secondary flows on the heat transfer of the blade and the effect of a heated and unheated endwall. Recently Borja Rojo et al. [20] has investigated endwall heat transfer in linear Cascade with IR thermography. They experimented by varying different configurations of OGV at two different Reynolds numbers. Their result found hot spots near the leading edge at every setting of OGV. More research is needed to apply infrared thermography in achieving data of endwall in heat transfer distribution.

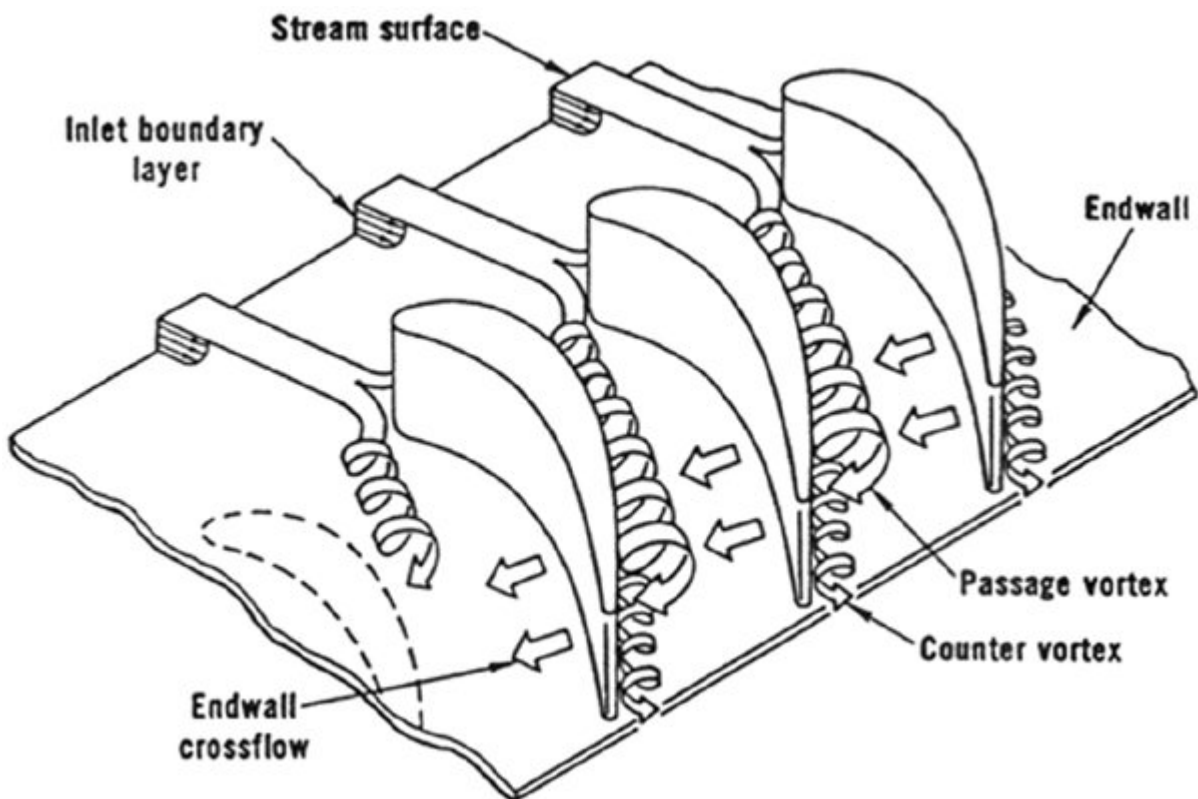


Figure 1 Endwall flow model by Langston et al. [2]

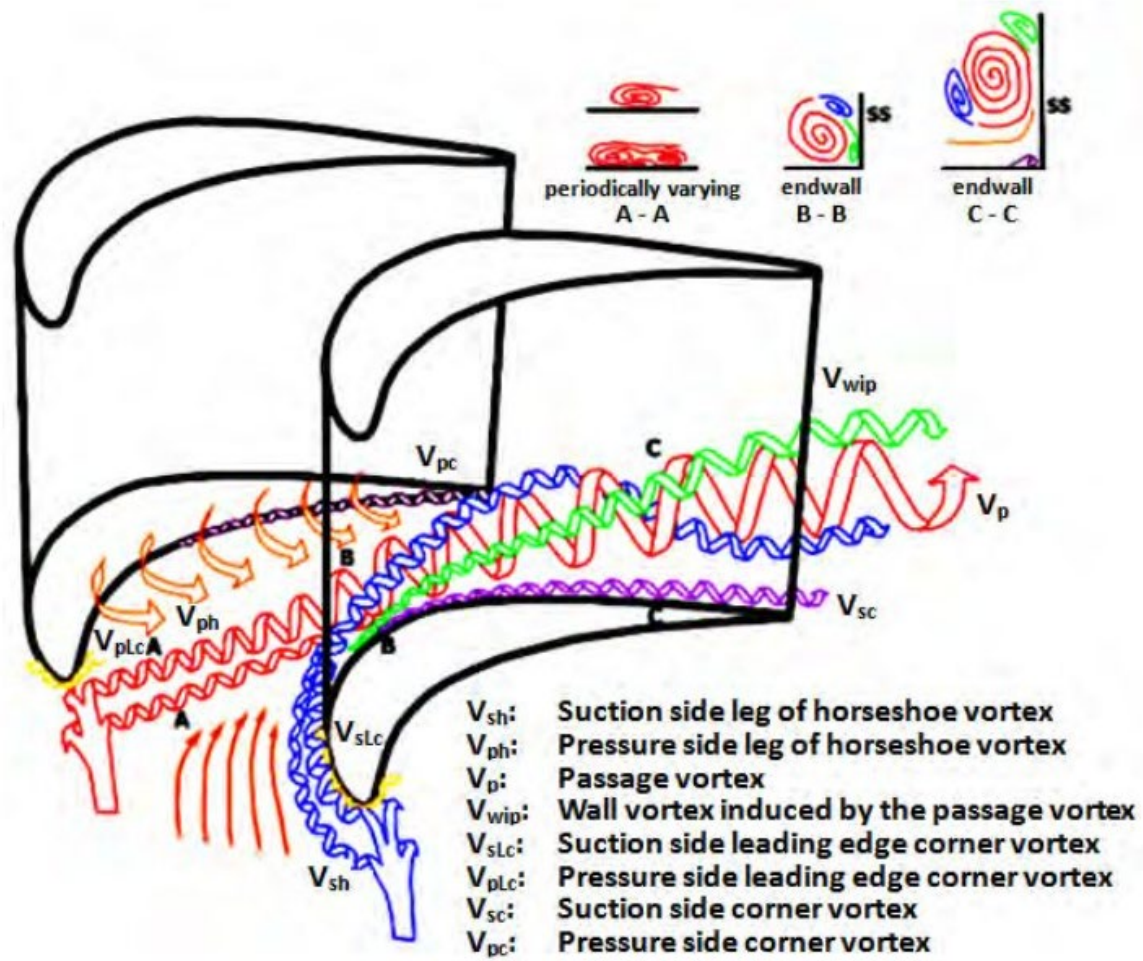


Figure 2 Endwall vortex model of Wang, Olson, Goldstein, and Eckert [4]

CHAPTER III

EXPERIMENTAL APPROACH

This chapter gives a detailed description of the University of North Dakota's large scale, low velocity cascade wind tunnel, as well as the construction and experimental procedure used to acquire free-stream pressure and temperature measurements on two different large leading edge instrumented cascade vanes. The wind tunnel is configured in a steady state blown down arrangement and shown in Figure 3. The wind tunnel components consist of the inlet filter box, a blower, two multi-vane diffusers, a heat exchanger, a mixer, a flow straightener, a screen box, a nozzle, the cascade test section, an exit diffuser, and an oblique diffuser. The nozzle component of the wind tunnel is interchangeably used to create different levels of turbulence ranging from 0.7%, using a low turbulence nozzle, to 17.4%, using the new high turbulence generator. All together five different turbulence levels were tested at three different Reynolds numbers ranging from 500,000 to 2,000,000.

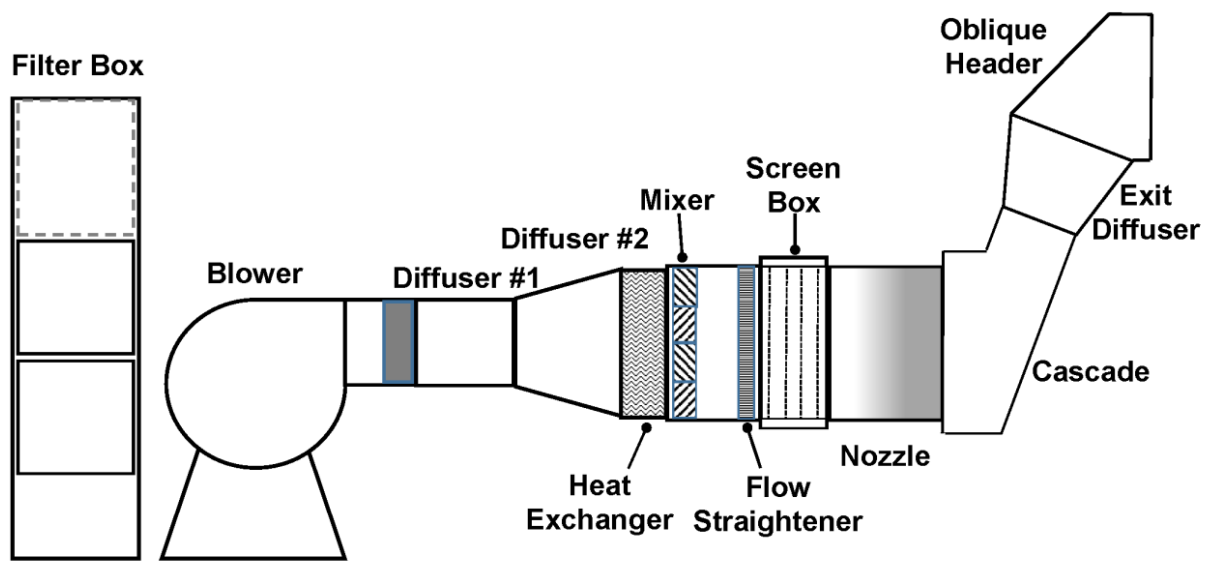


Figure 3 Large scale low-velocity wind tunnel

Filter Box

The University of North Dakota's large scale, the low-velocity cascade wind tunnel is used to force air through the test section in which is being studied. The air is first entrained through a filter box system which contains eight different Air Handler 6B640 industrial air filters to catch any particulates that could have been entrained with the air. Each of the filters is 24 inches by 24 inches and has an efficiency of 95%; it is essential to filter all of the particulates from the air to avoid any sort of disturbances while running the wind tunnel. The failure of filtering the air can cause surface roughness, which triggers alteration of the flow characteristics. There is a chance of collecting altered data if any disturbances of hot wires or pressure probes occur due to unfiltered air.

Blower

The setup is such that the filtered air, after traveling through the filter boxes, enters the blower. The blower that is used for our experiments is a New York 274-AF blower, which can deliver $6.6 \text{ m}^3/\text{s}$ of air at a 5000 Pa static pressure rise. The fan is powered by a 45 kW electric induction motor, which is controlled by a Hitachi variable frequency drive. The operator can finely tune the RPMs of the blower, which helps to keep the Reynolds number close to the desired value as the blower is attached to the variable frequency drive. The blower is shown below in Figure 4.



Figure 4 New York Blower used for Wind Tunnel

Diffusers

A two stage multi-vane diffuser is used so that the air can go through it to reduce the velocity of the air by expanding the flow and regaining some of the static pressure. The two-dimensional diffusers are used to increase the area of the wind tunnel from 16.5 inches by 24.25 inches (400.125 in^2) to 36 inches by 50 inches (1800 in^2), which is accomplished using two stages. The first diffuser expands the width from 16.5 inches to 36.0 inches, while the second diffuser increases the height from 24.25 inches to 50.0 inches.

Heat Exchanger

The air then passes through the heat exchanger to remove the energy added to the air by the blower. The 100-gallon plastic tank is used to store the water for the heat exchanger and circulated through the system by a $\frac{1}{2}$ hp centrifugal pump. At the bottom of the tank, there is a $1\frac{1}{2}$ inch polyvinyl chloride (PVC) pipe that carries the water from the tank to the heat exchanger. A ball valve places after the pump regulate the amount of water that enters the heat exchanger. The large plastic tank is used for the exiting water to travel back. A $1\frac{1}{4}$ inch PVC pipe takes the overflow water from the tank and places it into a drain on the floor. The schematic of the heat exchanger can be seen in Figure 5. The ball valve feature plays an important role in allowing the operator to control how much energy is taken out of the air depending on how hard the blower is working. As more energy was put into the air to propel the air at its higher Reynolds number, more energy needs to be taken out of the air at the higher Reynolds number. So, to keep the testing parameters as consistent as possible, more water needs to be cycled through the heat exchanger to cool the air. The system that we have in our lab is capable of developing a steady inlet temperature within a range of ± 0.2 degrees Celsius to create accurate and reliable steady state heat transfer testing results.

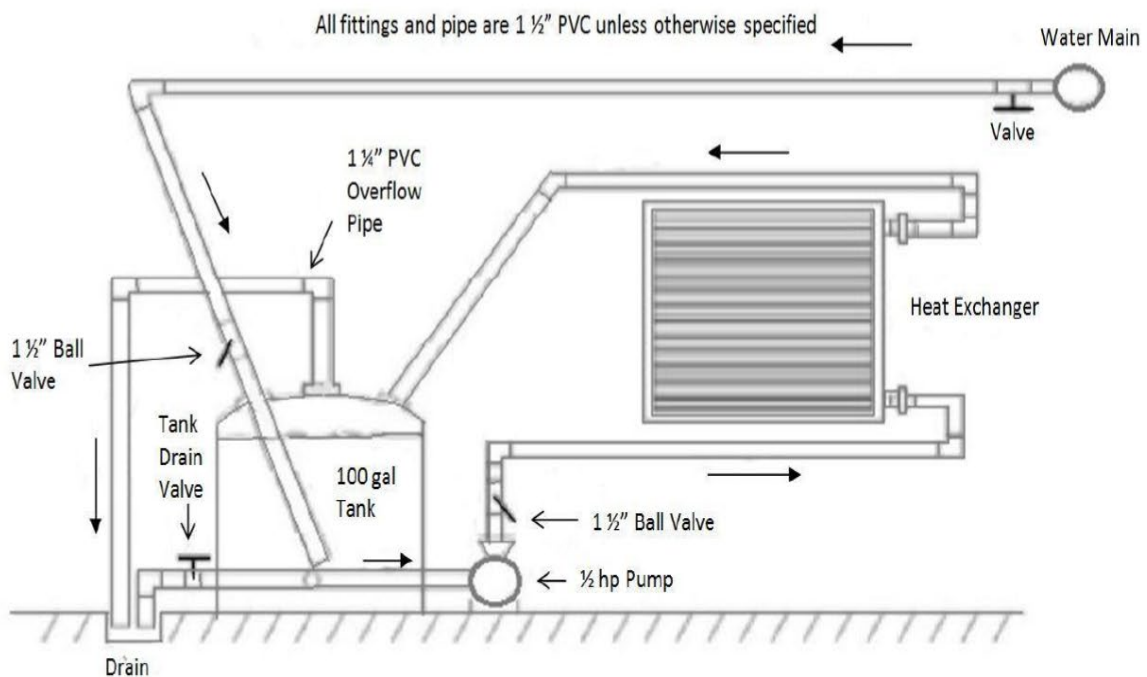


Figure 5 Schematic of wind tunnel heat exchanger

This heat exchanger can cause temperature stratification when running at higher Reynolds numbers due to two significant reasons. First, when running at the higher Reynolds numbers, there is a large amount of cold water being added to the heat exchanger system. Second, the heat exchanger is relatively large, so water added to the system takes time to warm before it travels back to the reservoir. In the high free-stream turbulence conditions, this is negated by the high levels of mixing that takes place downstream from the heat exchanger.

Flow Mixer

The flow mixer that was added to the system is located 13 inches downstream from the heat exchanger. Flow mixture is consists of 16 gauge steel and measures 36 inches by 50 inches. It contains ten rows of five fins turned 30 degrees off the plane perpendicular from the flow, causing the flow to be altered 60 degrees either right or left as it travels through the mixer, depending on which row the flow goes through. This helps mix out the spanwise temperature differences in the flow. Figure 6 shows the flow mixer inside of the wind tunnel.



Figure 6 Flow mixer

Straightener

A flow straightener was used to swirl in the mixing flow created by the flow mixer. The flow straightener helps to eliminate any effects that are caused by flow mixing and enhances the uniformity of the flow before it reaches the test section. The flow straightener is made from 1/8 inch diameter honeycomb aluminum with a streamwise length of 2 inches. It can be seen below in Figure 7.



Figure 7 Flow straightener

Screen Box

For reducing any velocity variations, a screen box is placed downstream of the flow straightener. Four large nylon screens are required to make the screen box situated 2 inches apart, one after the other. The screen box is shown below in Figure 8.



Figure 8 Screen box

Turbulence Generators

For this facility, three different nozzles or turbulence generators were required to create up to seven different turbulence levels. The different turbulence generators were designed to facilitate a range of turbulence levels from 0.7% to 17.4%. The three different nozzles that were used during the experiments are a low turbulence nozzle, a mock aero-derivative combustor, and a new high turbulence aero-derivative combustor simulator.

Low Turbulence Nozzle

The four lowest turbulence levels which were used in this experiment have been generated by using a low turbulence nozzle. The nozzle's 3.6 to 1 area reduction was developed to create a smooth flow transition. This 0.7% turbulence intensity inlet flow has been created by placing the

exit of the low turbulence nozzle directly coupled with the cascade. The low turbulence nozzle can be seen in Figure 9.

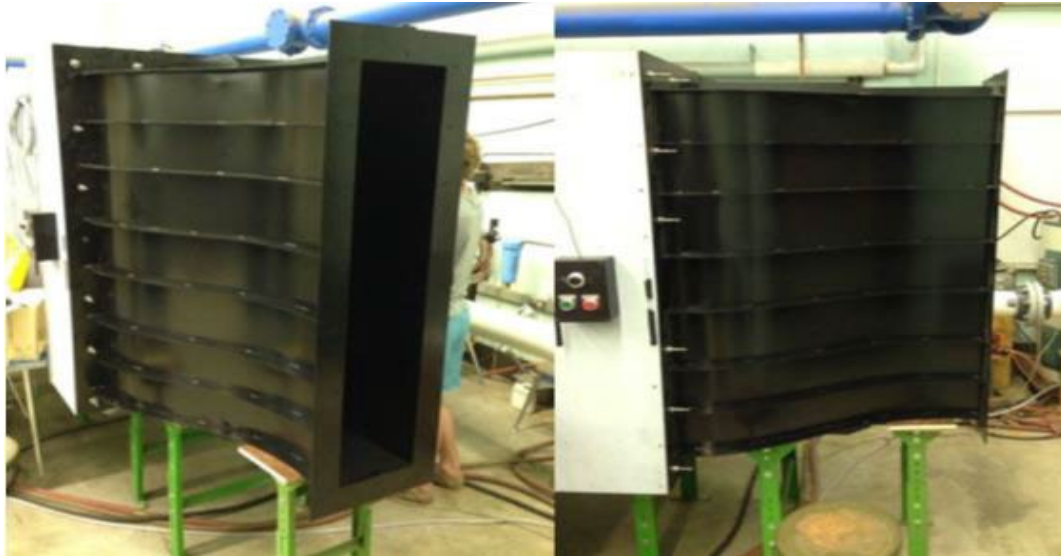


Figure 9 Low turbulence nozzle

The rest three turbulence levels ranging from 3.5% to 8.1% can be developed by placing different grids in a rectangular spool place at different positions based grid mesh spacings. A large grid can be placed at 10 mesh lengths upstream from the cascade vane inlet plane or the small grid could be placed at 10 or 32 mesh lengths upstream from the vanes. The 36 inch long rectangular spool is placed at the exit of the nozzle and is coupled to the cascade. $\frac{3}{4}$ inch acrylic walls are required to make the spool which maintains a constant 10 inch by 50-inch cross-sectional area, identical to the exit area of all three nozzles. The small grid which is made up of 0.25-inch square aluminum bar spaced at 1.25 inches, or five bar widths resulting in a 64% open area grid can be placed in one of two different positions. Turbulence levels of 3.5% can be

created by placing the small grid 40 inches away from the vane leading edge plane. This condition is called the small grid far configuration. The small grid near configuration, which can create a turbulence level of 7.8%, is developed by placing the small grid 12.5 inches away from the vane leading edge plane. The small grid near and far configurations can be seen in Figure 10.



Figure 10 Small grid far configuration (left) and Small grid near configuration (right)

The large grid, which is made from 0.5-inch square aluminum bars with a five bar width spacing, is used to create a free stream turbulence level of 8.1%. The grid is placed 25 inches away from the surface to get the desired turbulence level. The large grid turbulence configuration can be seen in Figure 11.

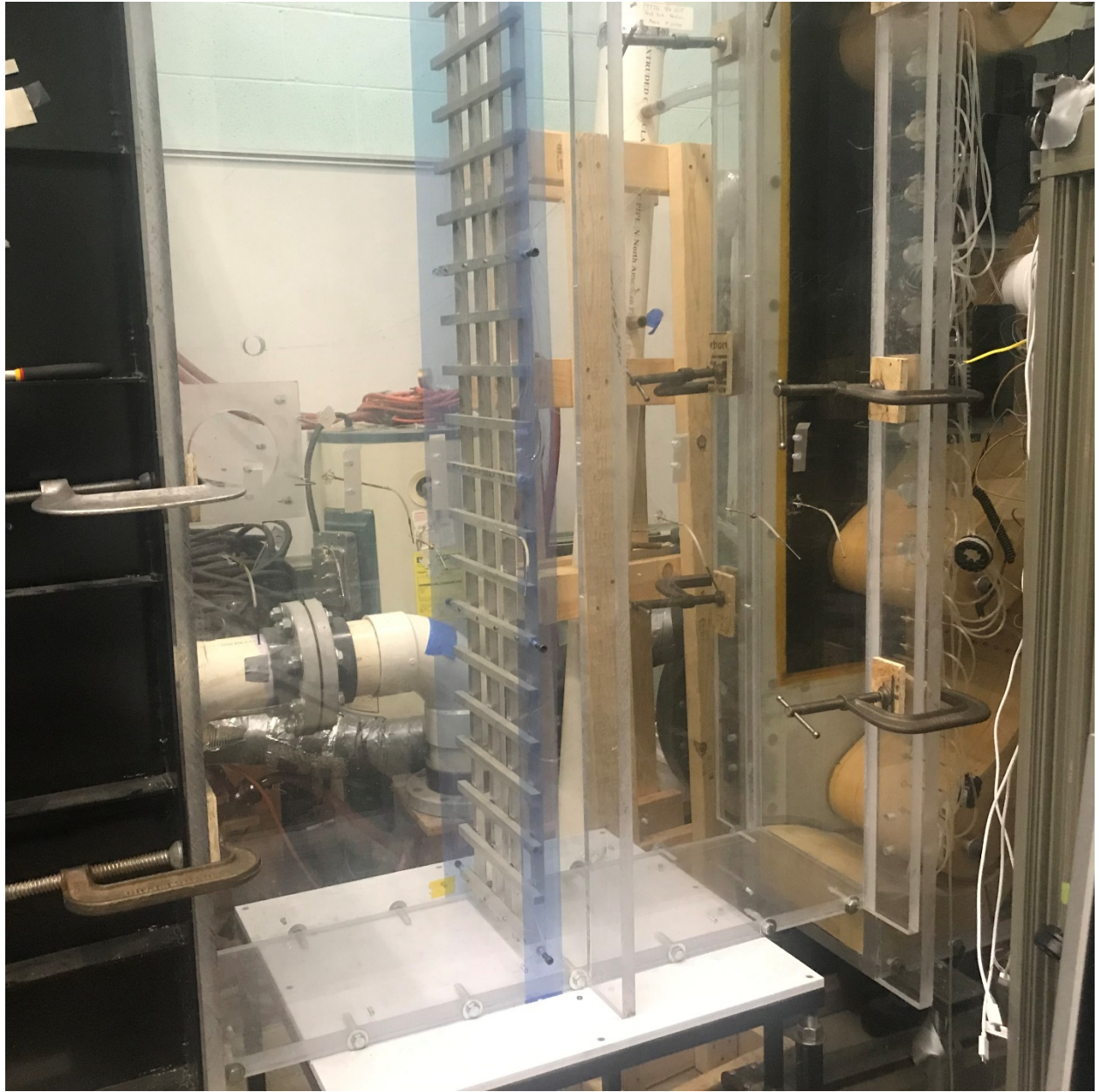


Figure 11 Large grid configuration

Mock Aero-derivative Combustor

The next two turbulence levels can be created by using mock aero-derivative combustors, which are a kind of nozzle capable of generating turbulence without any grid. When the cascade test section is placed directly against the nozzle, it is capable of creating a turbulence level of 13.7%. When the decay spool (rectangular spool) is placed in between aero-derivative and test cascade, the turbulence level drops to 9.2%. The mock aero combustor can be seen in Figure 12.

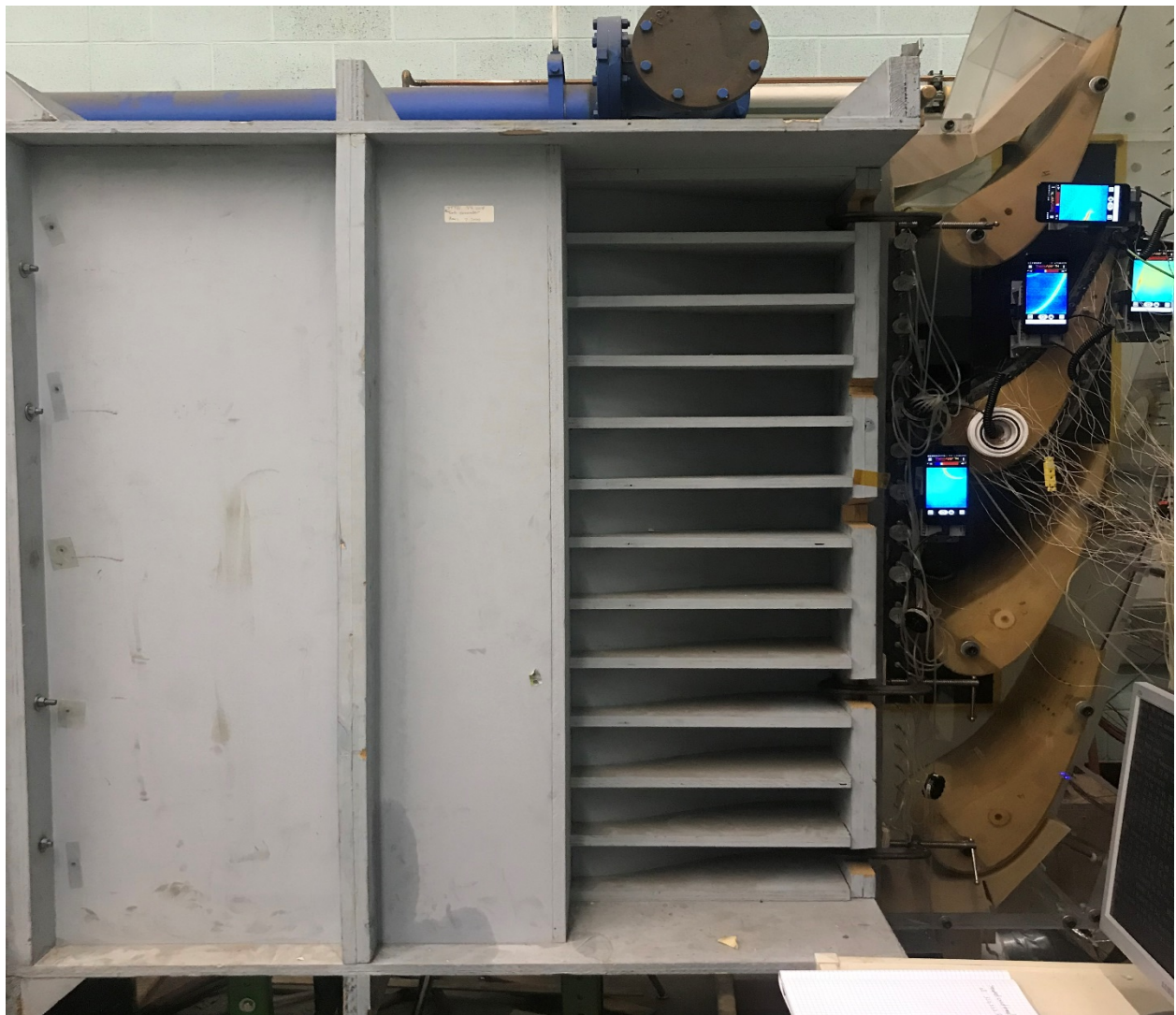


Figure 12 Mock aero-derivative configuration

High Turbulence Nozzle

The highest turbulence generator, which has a specification of having minimal area reduction, as well as the same exit area as other nozzles, can be capable of creating free stream turbulence of 17.4% when it is directly placed against the testing cascade. It has been shown in Figure 13.



Figure 13 High turbulence nozzle configuration

Cascade Test Section

The air enters the large scale linear cascade after passing through any of the three nozzles and the many different turbulence generating configurations. The cascade is inspired by a modern mid-sized industrial gas turbine and is created on an eleven to one scale. The objective is to simulate the airfoils and endwalls in an industrial gas turbine. The cascade test section is composed of four vanes and three passages. Many features of the cascade are in place to check that the two-dimensional aerodynamic data are accurate and repeatable. The four vanes are cast from an epoxy; three slave vanes are bolted into the cascade, as well as an interchangeable vane. An endwall heater, three endwall coolers, a row of inlet pressure taps, and a row of exit pressure taps, two adjustable tailboards, and an upper and lower bleed flow adjustment are included in the cascade. The entire configuration of the cascade can be seen in Figure 14.

The four vanes, three linear passage cascade test section, was fabricated from 1-inch thick acrylic. The advantage of using acrylic is it allows the operator to see into the cascade when testing was being conducted and provides a rigid structure that doesn't conduct heat. Detailed dimensions of the cascade are shown in Appendix A. The 30 inlet and exit pressure ports are one of the essential features of the cascade. The inlet pressure ports are placed at one-quarter axial chord upstream from the leading edge of the vanes. Similarly, the exit pressure ports are placed at a one-quarter axial chord downstream from the trailing edge. Ten probe access ports were also drilled through the endwall to help monitor the inlet pressure and temperature conditions of the cascade. The flow is turned between 74 and 75 degrees before exiting the cascade and directed to the exit diffuser.

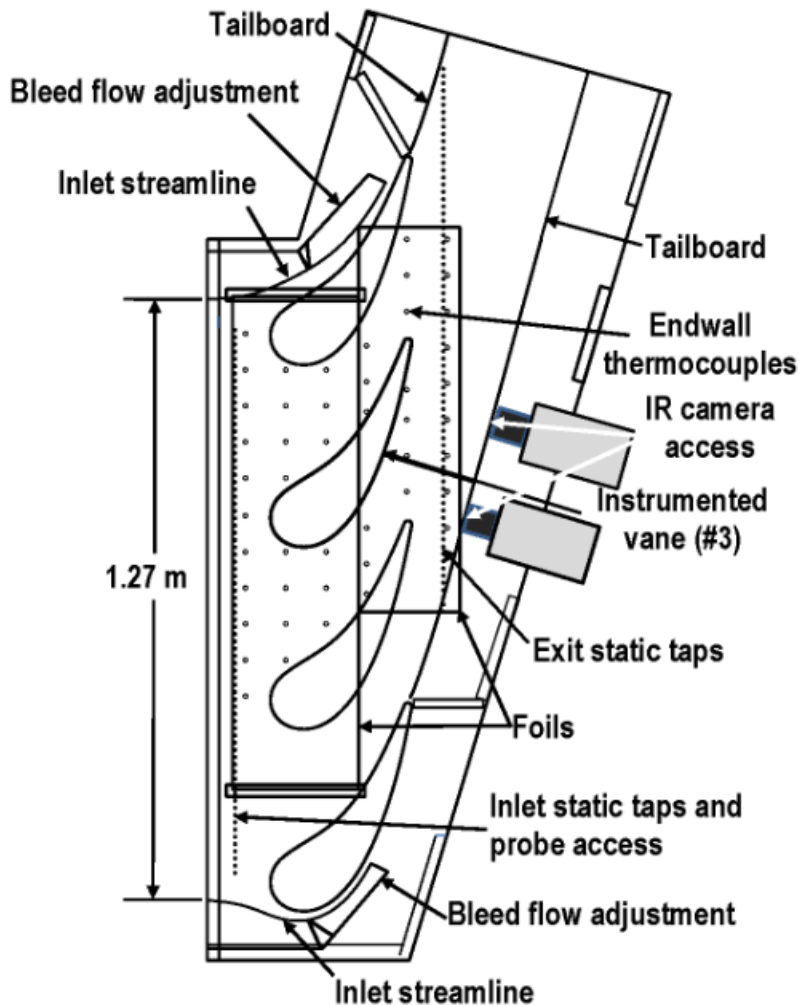


Figure 14 Layout of Cascade

Bleed Flow Adjustments

Two bleed flow fixtures (Upper and lower bleed flow) were installed to mimic the upper and lower flow boundary conditions that the vanes themselves provide in the cascade. They were made of an isocyanurate foam core and covered with a very thin, 1/64 of an inch, and flexible epoxy fiberglass (G-10) board. The shapes of the vanes were designed to ensure that the inlet

flow entered along the projected streamlines and keep the flow as uniform as possible in the cascade. The bleed flow vanes can be adjusted to control the flow rates along the top and the bottom vane, which is critical to maintaining the desired streamlines on the upper and lower slave vanes.

The bottom bleed flow adjustment can be achieved by cutting a slot, and flow adjustment has been made by nylon rod attachments at the back of the fixture. A piece of adjustable acrylic placed on top of the vane performs the same function as the cutout slot on the lower vane by sliding in and out to meter the flow around the vane and help create the desired inlet uniformity.

Both the upper and lower bleed flow vanes can be seen below in Figure 15.



Figure 15 Lower tailboard (left) and upper tailboard (right)

Exit Tailboards

The two exit tailboards were attached to the trailing edges of the top and bottom slave vanes in the cascade to ensure that there is exit periodicity in the flow. The tailboards are flexible enough to adjust the placement along the streamlines of the flow, accounting for the growth of the boundary layer along the tailboard themselves. 3/16 inch polycarbonate is needed to fabricate the tailboard. Tailboards are attached to the top and bottom slave vane through ¼ inch wide by ½ inch deep groove that was machined into each of the vanes trailing edges. After inserting into the grooves, the tailboards fastened in place with an RTV silicone sealant.

The bottom tailboards was more flexible since it was able to be placed in five different positions according to the placement and adjustment of the tailboard. Top tailboard could be placed by attaching nylon rods in two separate sections. Polycarbonate sheet is attached at the top edge of the tailboard to assist in the adjustment of the tailboards at the cascade exit.

IR Camera Mounting System

For this experiment, commercially available compact and light-weight infrared cameras "Therm app" has been procured because of their high 384*288 pixel resolution and accompanying software allowing digital temperature information. The cameras are based on uncooled microbolometer technology, which allows for versatile use in almost any environment without the need for cooling equipment. After careful consideration, it was decided that five therm app cameras were sufficient to cover the entire passage, which is crucial to acquire overall coverage of endwall by image stitching given the passage's periodic nature. The therm app camera can be seen in Figure 16.



Figure 16 Therm app camera

This therm app camera comes with a USB cable that has to be connected with an android device featuring an operating system 4.1 or above.

Camera mount

The camera holder has been designed to mount the camera on the endwall, shown in Figure 17. The objective is to capture a streamwise and spanwise image of the endwall from upstream to downstream from some fixed location. The camera mount has to be designed to make the cameras rigid in one fixed place. The five-camera mounts for five cameras are built by using 3D printing. After installing the camera mount in the endwall, to ensure rigidity, the camera mount is

drilled .19 inches at the side of both ends to insert a set screw while mounting against the acrylic wall. The geometric dimension of the camera has been given in Appendix B.

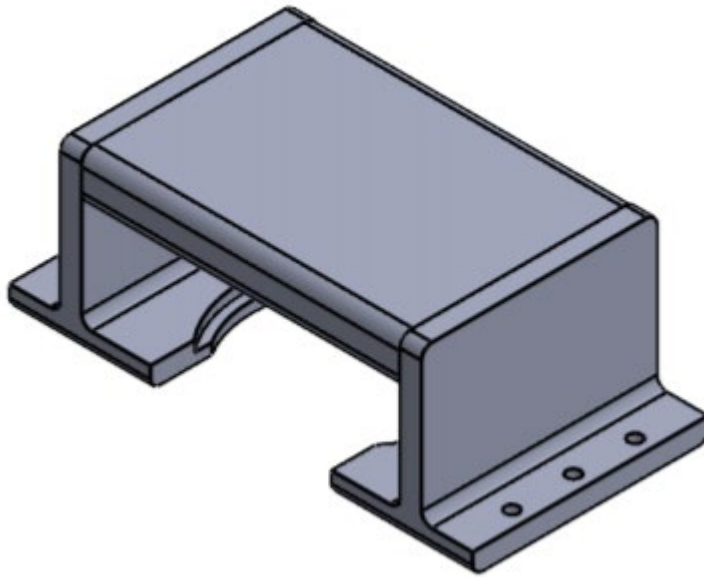


Figure 17 Camera mount

IR Window and Window Holder

Anti-reflective coated zinc selenide windows were purchased to create an interface between the test section airflow and the camera lens. The 1-inch diameter zinc selenide window transmits the desired wavelength range of IR radiation to the camera lens. Zinc selenide window is also used for its low absorptivity and highly resistant to thermal shock, which is crucial to ensure a better quality image. An aluminum holder was machined in the UND machine shop to hold the window in place. Detailed drawings of the window holder are available in Appendix A. The lens holder and the zinc selenide viewing window is in Figure 18.

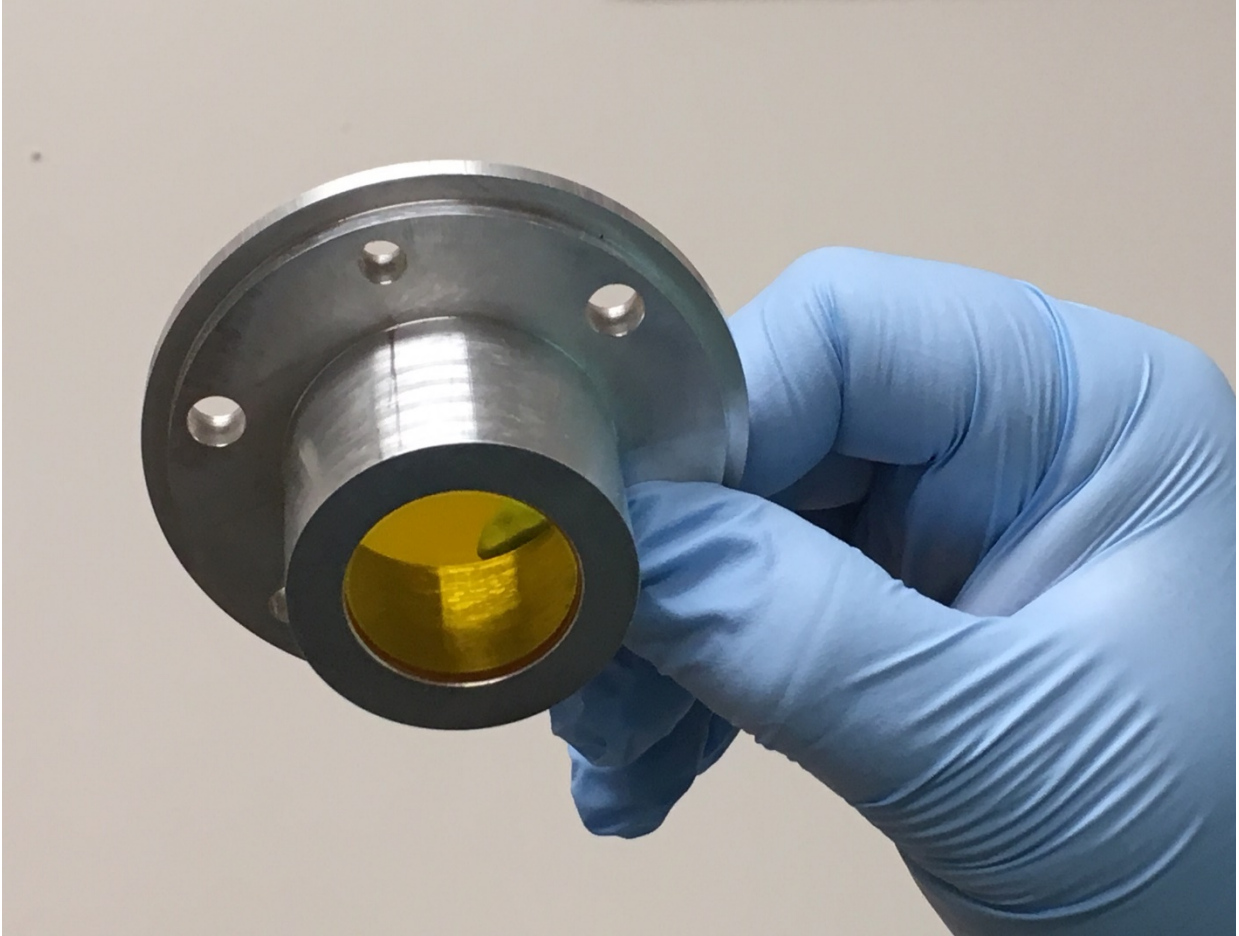


Figure 18 The window holder and zinc selenide window

Installation

Five-positions on the endwall were selected, which gave better coverage to acquire an overall image of the endwall surface. A round a 1.5-inch diameter hole was cut in the acrylic wall using a hole saw and router at the five selected spots. Then the window holder, which is made of aluminum, was placed on the endwall. Then the camera mount where the camera is placed beforehand was installed onto the mount in the acrylic wall. The experimental setup can be shown in Figure 19.



Figure 19 Experimental setup of the IR Cameras

Turbine Vanes

The vane used for the experiment was designed to possess a relatively large leading edge and an aft loaded suction surface. The vanes leading edge was intended to have a 5.2-inch diameter on a line that passes through the stagnation point on the vane. The reason behind choosing the large leading-edge design was to help reduce the heat transfer levels in the leading edge area of the vane, along with creating more room for the leading edge to be internally cooled. The aft loaded suction surface facilitates the boundary layer acceleration, which eventually minimizes the growth of the boundary layer, and delaying the transition of the flow.

The vanes in the cascade have a chord length of 19.590 inches and are vertically spaced 15.152 inches apart from each other. The leading edge to trailing edge axial distance for each vane when it is placed in the cascade is 11.198 inches, which means each vane is situated at a setting angle of 54.42 degrees. After each vane was cast, they were cut down to a precise height of 10.0 inches and placed in the cascade. Three of the slave vanes were bolted into the cascade. The other vane, which is the third vane from the bottom, named instrumented vane, can be easily inserted and removed from the cascade through a window cut into the endwall. Two different instrumented blades for the cascade is required for this experiment, one of them is a pressure vane, the other a heat transfer vane.

Pressure Vane

The pressure vane is one of two instrumented vanes that were constructed for the experiment in the cascade. Forty pressure taps were placed on the outer edge of the vane to obtain an optimal

vane surface pressure distribution. After constructing from 1/16 inch brass tubing, the pressure tubes were placed 1/16th of an inch below the surface of the vane, meaning that they were glued to the foam core of the pressure vane. Brass barb fittings were soldered onto the ends of the pressure tubes to help with the ease of assembly for the pressure tubing onto the pressure tubes. 0.040-inch holes were drilled into the brass tubes at the mid-span of the vane, to sense the pressure distribution along the surface of the vane. This location was selected by ensuring that the flow, which the pressure taps captured, had little to no disturbance from the endwall of the cascade. The pressure was rapidly changing near the stagnation region, and hence a concentration of the pressure taps was located near this region to capture the flow behavior in this area. The pressure ports were placed further from one another in areas where the pressure drop was more linear. Pressure vane can be seen in Figure 20.



Figure 20 Pressure vane

Heat Transfer Vane

The second instrumented vane is the heat transfer vane, which is important to measure heat transfer distribution. This vane was cast with 55 fine wire type K thermocouples located at the mid-span of the vane to obtain a full surface temperature distribution over the vane.

Commercially fabricated 9.93 inches by 42-inch constant heat flux Inconel foil has been used to wrap the vane. A 0.05 mm thick (0.00197 inches) layer of Kapton was bonded to the foil and was backed with a high temperature pressure sensitive adhesive, which allows the foil to adhere to the surface of the vane. Two copper bus bars are soldered onto the ends of the foil for even distribution of the current throughout the foil. To minimize any aerodynamic blockage that could occur from the surface roughness on the vane these bus bars were placed into the pressure and suction sides of the trailing edge of the vane into machined grooves. The heat transfer vane can be seen in Figure 21.

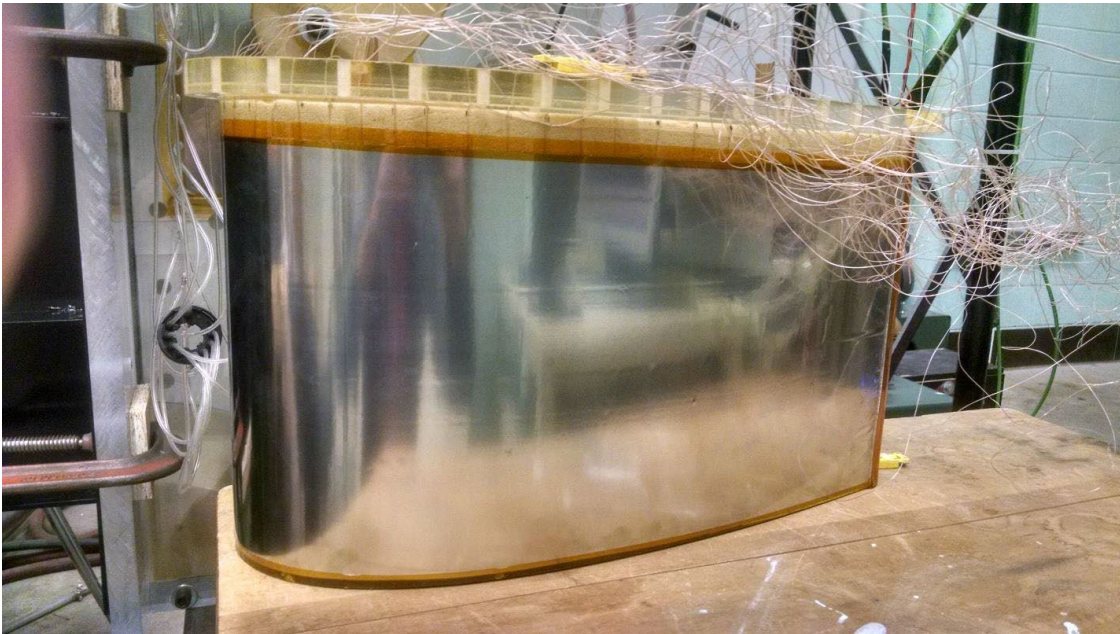


Figure 21 Heat transfer vane wrapped in Inconel foil

The Endwall

The cascade has two distinct endwalls, a near endwall, and a far endwall. The pressure taps and access ports drilled into the surface of the near endwall. The 30 inlet pressure ports, placed at one-quarter chord upstream from the leading edge plane, help to ensure good inlet flow uniformity. Similarly, the 30 exit pressure ports, located one-quarter chord downstream from the vane's trailing edge plane, help establish the exit periodicity of the flow exiting the cascade. A 1/8 inch hole was drilled vertically through the acrylic wall until 0.05 inches from the end of the acrylic endwall to construct each of the pressure ports. A pressure port (used for taking pressure reading) was created by using .040 inch drill bit to penetrate the surface of the endwall. The pressure taps themselves were fabricated from telescoping brass tubes that were soldered together. The pressure tap of each port was made from three different one-inch long brass tubes: 1/8 inch diameter tube, followed by a 3/32 inch diameter tube, and finally a 1/16 inch diameter tube. These brass tubes were soldered together, and barbed tube fittings were soldered onto the end, which creates an easy way to attach and detach the pressure tubes from the cascade. They were then inserted into the holes that were previously drilled into the endwall of the cascade and epoxied in place. There were ports in the cascade to monitor inlet total pressure and total inlet temperature of the flow. Two type K thermocouples was inserted through the endwall to determined the inlet total temperature. Before inserting these thermocouples, the temperature probe was inserted through a 1/16 inch brass tube to increase the rigidity of the thermocouple. The near-end wall can be seen in Figure 22.

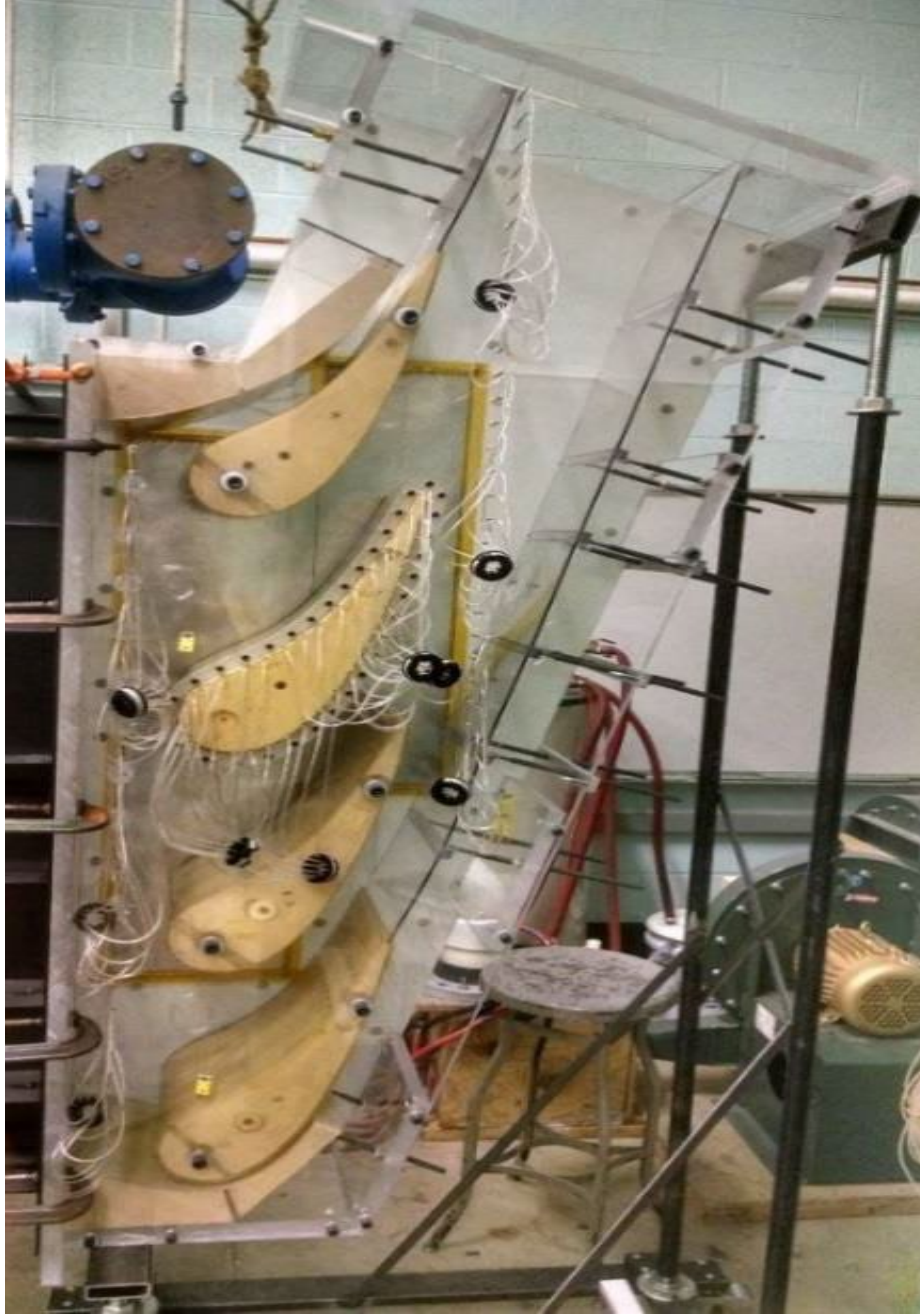


Figure 22 Cascade near endwall

Apart from this, the near endwall included a window cut into the surface to facilitate the desired vane installation. The window was cut to a 1/32 inch larger radius than the size of the vanes positioned in the cascade so that the instrumented vanes can be placed in the same location each time one is switched out for the other, hence ensure accuracy between the different tests that were conducted. The far endwall included two different layers: the outer layer is composed of the 1-inch thick acrylic. The area of the constant heat flux foil of the cascade was kept rigid by bolting two 1 inch by 2-inch aluminum bars onto the endwall. This rigidity helps the cascade to be fixed in its place. The inner part of the endwall was composed of both the 1-inch thick acrylic and 1-inch thick isocyanurate foam to provide insulation to the rest of the cascade from the constant heat flux foils. Inside the foam, three endwall coolers, or heat sinks, were installed to help keep the temperature of the endwall and the temperature of the surface under the vanes constant throughout the experiment. More information on the construction of the endwall heat transfer system can be found in Appendix C. The foam and the endwall coolers were then covered with a thin sheet of epoxy fiberglass board, which was placed over the foam to provide a surface to adhere the constant heat flux foils onto the endwall surface. The endwall has two foils in rectangular shape: the large foil (42.5 inches by 10 inches) and the small foil (32 inches by 8 inches). After the foils were attached to the endwall, the high-temperature tape was placed on the edges of the foils to minimize the disturbances of the flow. Under the constant heat flux foils, 48 thermocouples of the known location were placed on the surface of the endwall to conduct an in situ calibration technique for an accurate temperature profile of the two passages surrounding the instrumented vane.



Figure 23 Cascade far endwall

The primary purpose of the experiment is to observe heat transfer distribution on the endwall by applying the thermography technique. The endwall surface is painted matt black by using acrylic paint to enhance the emissivity of the surface to get a better result from the thermal image. An airbrush is used to paint the endwall to get a smooth finish on the surface, given that any sort of surface roughness can alter the temperature distribution. Gold dots were painted on the endwall surface in a 3 inch by 3-inch grid starting from an edge of the foil, which will help to establish a reference point during the data analysis procedure. The painted enwall surface can be seen in Figure 24.



Figure 24 painted enwall surface

Exit Diffuser

After passing through the linear vane cascade, the air enters the exit diffuser, which directs the air up toward the ceiling and into the oblique diffuser, placed on top of the exit diffuser. The function of the exit diffuser is to regain static pressure and decrease the velocity of the exiting air. The exit diffuser was designed to reduce the speed of the exiting air by half and recover as much static pressure as possible. The outer shell of the diffuser is composed of 1 inch thick acrylic and is designed to match the size of the exit of the cascade. The diffuser has movable outer walls that were made from 3/16 inch thick polycarbonate to adapt to the changing exit area of the cascade. The three inner vanes were placed in grooves cut into the sides of the walls in the diffuser. The vanes were adhered into place to ensure rigidity during the tests. The exit diffuser can be seen in Figure 25.



Figure 25 The exit diffuser

Oblique Diffuser

Even though an exit diffuser's usage made the exiting air's velocity lower, it is still deemed high in terms of the safe operation. The exiting air was directed toward the ceiling, which made the lighting fixtures more susceptible to the high velocity exiting air. Considering these light fixtures is critical while testing because, without them, the lighting in our testing area would have caused safety problems, especially when taking pictures to document heat transfer distribution of endwall testing on the cascade. Therefore, to avoid this kind of problem, an oblique diffuser, shown in Figure 26, was attached to the cascade to slow once again the air exiting the cascade and redirect the airflow 90 degrees, ensuring that it wouldn't hit the light fixtures above. The oblique diffuser was designed with eight vanes and nine passages, which turned the air 90 degrees as the air traveled through the entirety of the diffuser. It was constructed out of $\frac{1}{2}$ inch AB plywood to make it light-weight, which can be easily placed on top of our cascade. We felt that the oblique diffuser needed to be light because our cascade is approximately 12 feet tall, and for the ease of assembly, a lighter oblique diffuser would be better.



Figure 26 The oblique diffuser



Figure 27 Power supply

Pressure Measurements

The pressure measurements of this experiment were acquired through two different Rosemount pressure transducers. The smaller one is capable of measuring differential pressures up to 250 Pa (0.036 Psi), where the larger one measures differential pressures up to 5000 Pa (0.725 Psi) with an accuracy of $\pm 0.1\%$ of the full scale that they are measuring. The pressure

The Data Acquisition System

High quality endwall heat transfer distributions data is obtained for this experiment by using a Hewlett Packard 3497A data acquisition system. This system is capable of reading 100 channels of DC voltage measurements and was interfaced with a computer to acquire the data for farther analysis.

Power Supply

The power supply was required to acquire the heated endwall heat transfer distribution. The endwall foil and also the heat transfer vane foil has been powered by the power supply. The current from the main power supply is determined using a 0.001-ohm precision constant shunt resistor, which was connected to the power supply in series with the foils in the cascade. 10 AWG stranded wire supplies current to the Inconel foils. The temperature of the endwall can be controlled by adjusting the current and voltages of the power supply. The second power supply was used to supply power to the 8" by 32" foil on the endwall. This secondary power supply is connected to the smaller endwall foil through a 0.005-ohm precision shunt resistor, which makes the distinction from the main power supply. transducers were connected to 48 port pressure scanner, composed of 48 12VDC solenoid valves, 1-44 are connected to the low side of the transducers, and 45-48 are connected to the high side.

Temperature Measurements

All of the temperature recordings for this project were taken using type K thermocouples. Each of the thermocouples was cut to the length of approximately six feet away, so it connects the heat transfer vane, nearly four feet away, to the thermocouple jack panel. The endwall thermocouples are also connected to the jack panel. The thermocouples placed on the endwall needed wire jumpers to reach the data acquisition tower, which can be seen in Figure 28. The accuracy of the

temperature measurements of all thermocouples was made by referencing to an ice bath through a passive constant temperature junction. The ice bath thermocouple was kept in a glass tube, which had mineral oil on the bottom to maintain a uniform temperature inside the tube. The glass tube was placed inside the thermos, and the thermos sealed to maintain its temperature throughout the entire testing procedure. The ice of the icebath had to be changed every two days to ensure the accuracy of the results; otherwise, the melted ice will give us overestimated readings, which is undesirable and inaccurate.



Figure 28 Data acquisition tower

Procedure

The acquisition of endwall heat transfer distribution for the wind tunnel has been executed in several steps. First, the blower had to be turned on, and the room's barometric pressure had to be measured. When that was done, the quick basic program FATEWHT could be turned on, and the barometric pressure could be entered into the program, and the pressure sensors could be zeroed. When the pressure sensors were zeroed, the program opened itself. The desirable Reynolds number has to be adjusted by rotating the knob on the potentiometer to control the variable frequency drive. The heat exchanger had to be turned to maintain a steady inlet temperature for the system. In the case of a Reynolds number of 500,000, the heat exchanger did not need to be activated because the energy added to the air by the blower was not sufficient to frustrate the inlet temperature's steadiness. For the remaining two higher Reynolds numbers, the heat exchanger had to be activated; otherwise, it altered the inlet temperature. The blower ran until steady-state occurred for the system at the given Reynolds number being tested. After waiting for about half an hour, a steady-state condition was reached then the two different types of tests could occur.

The pressure tests were run at first. This test was acquired to gain confidence regarding the cascade set up and observed the inlet, exit, and vane pressure distributions within the cascade, which will give the information about aerodynamics produced. The proper quick disconnect was connected to the pressure scanner to acquire either the inlet, exit or vane static pressure distributions. The appropriate subroutine had to be selected in the program to take one of the pressure tests. The program is set up, so typing in the number 3 led the system to take inlet pressure distributions. The number 4 led the system to take exit pressure distributions, and the number 5 led the system to take a vane pressure distribution. The system reads one port's

pressure, then it closed that port and moved on to the next one until all of the pressure ports were covered. A file was saved to the computer, which recorded all the pressure readings for further analysis. After completion of a pressure reading, endwall temperature data were taken. These data were taken in both adiabatic (heated system off) and heated condition (heated system on). For each case, an adiabatic data set was recorded at a steady state for the given test conditions; Then, the heater has to be turned on to measure the heated surface. The main power gave the power to the larger endwall foil while the second power supply gave power to the smaller endwall foil., The second power supply provides 62% of power to that of the main power supply to maintain a constant endwall heat flux. During the heating condition, to avoid overheating the endwall surface, the system had to be steady-state with air blowing over the foils. When the heated endwall reached steady-state, the endwall temperature can be monitored by typing 2 in the quick basic program. While monitoring endwall temperature condition, one thing has to be kept in mind that the differences of inlet total temperature and the maximum temperature should be no more than 15 degrees Celsius; otherwise the differential growth between endwall and foil when cooled down will jeopardize the smoothness of the foil. The thermocouple temperature distribution of the endwall could be monitored by pressing option 10 in the program. Once the data were taken, the file was saved to analyze further.

The third and final step is to take IR images of five cameras, which will cover the vane passage. Since we are concerned about in situ calibration for better accuracy, we took endwall pictures by manually clicking five cameras simultaneously right after recording the thermocouple temperature distribution of the endwall for each run. Hence, the second and the third step is done simultaneously to make a comparison with better accuracy. The second and third procedures are conducted for three Reynolds numbers and varying turbulence intensity at the adiabatic

condition. The same process was repeated for the heated condition as well. Both adiabatic and heated heat transfer distribution measurements for different Reynolds numbers and turbulent conditions can be acquired when the wind tunnel reached a steady-state after turning on the blower. Once all the IR images were taken for various conditions, the images were transferred into PC to export data from those images, which can be scrutinized for image processing. After the thermocouple data were taken, the power of the heater was turned off, and the system continued running until a steady state was reached again. Afterward, the blower was turned off, and the program was terminated for the day.

Image Processing

The image processing has been started with addressing and correcting the temperature drop in the edge of the image, which is called the “Fisheye effect.” To determine fisheye correction, compensation for the fisheye effect was developed and was able to use the image processing toolbox within MATLAB to remove the fisheye effect. The change in temperatures at the periphery was addressed by creating a compensation matrix and subtracting the compensation matrix from each image. The compensation matrix was created by using a picture of an isothermal surface and determining the relative offset of each pixel relative to the actual temperature of the surface.

At the beginning of each testing session, the adiabatic thermocouple temperature was recorded for all the 47 points of thermocouple sensors located on the endwall surface. Among them, only 25 thermocouple sensors were located within the camera field of view. Each of the camera (total 5) has equal dimension of the field of view which is 7.7 inch \times 9.2 inch (Corresponding to 288 \times 384 pixels in IR image). The thermocouples were assigned a number that was used to reference the sensors within the study. The location and number are shown in Figure 29. The dot within the

circumference circles indicates those 25 thermocouples, which also have the reading from the IR camera.

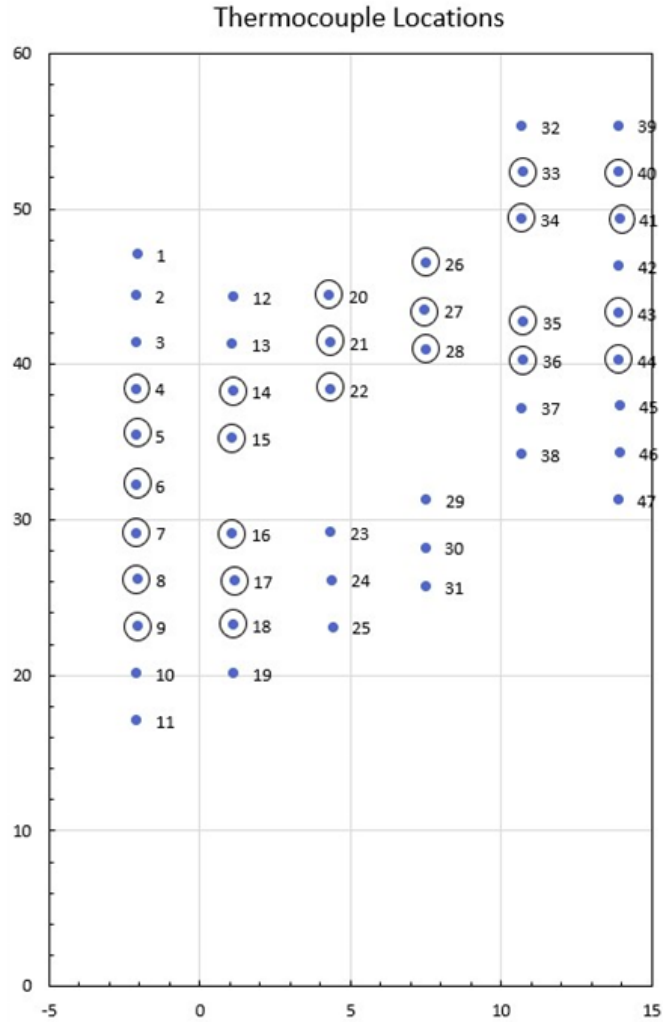


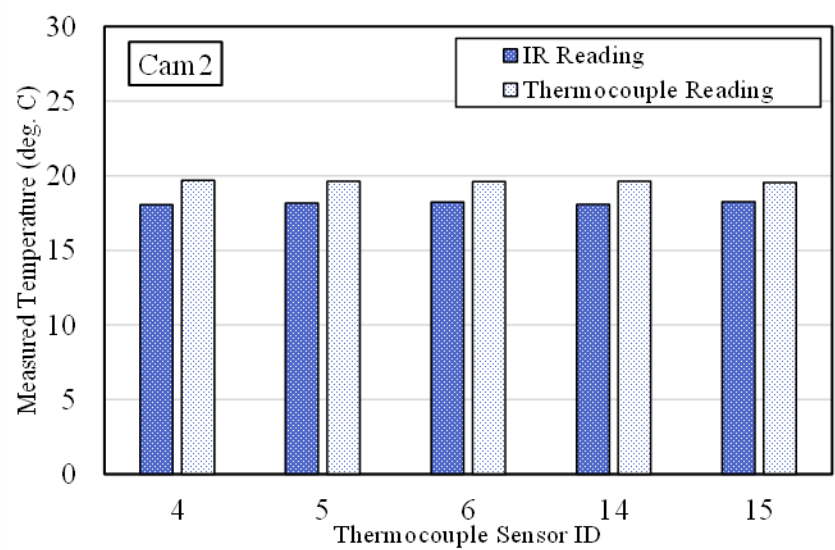
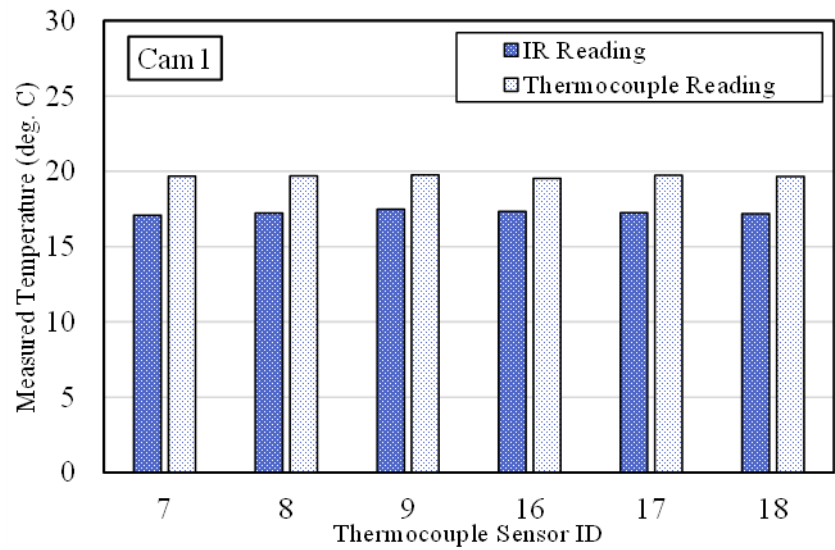
Figure 29 Location of the thermocouples along the endwall surface

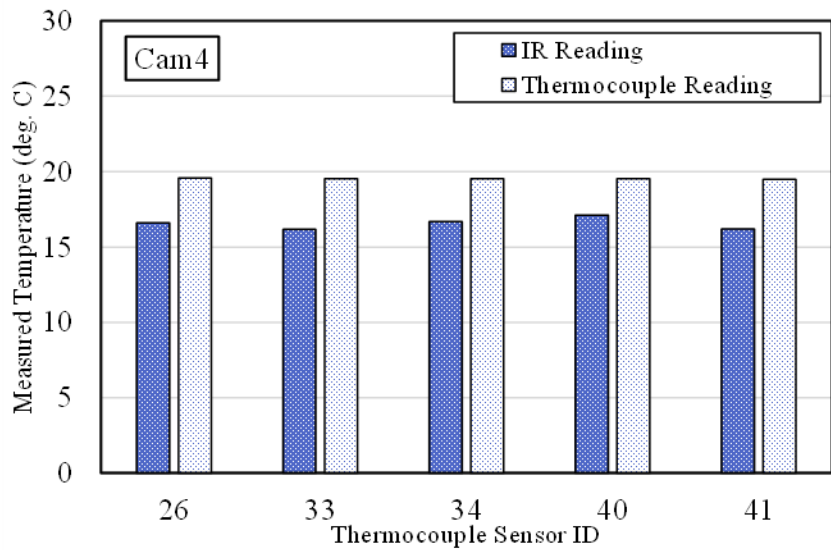
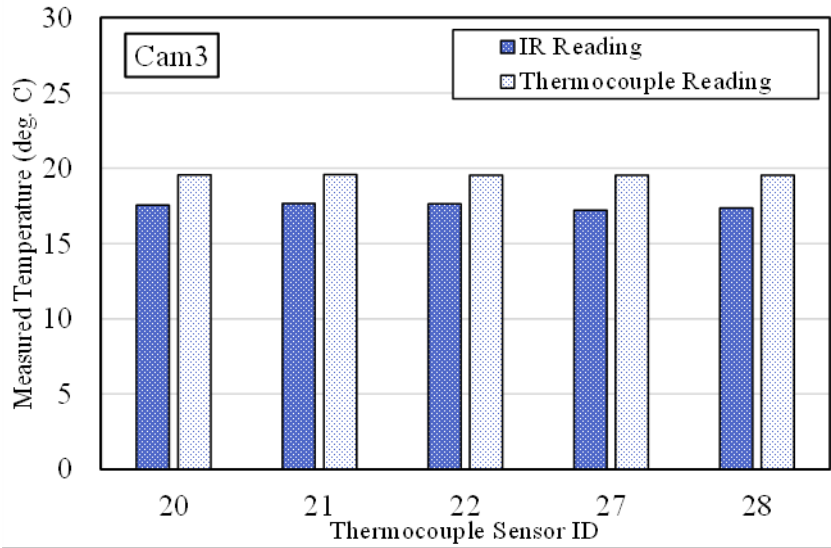
The following table indicates the number of thermocouples and camera field of view information.

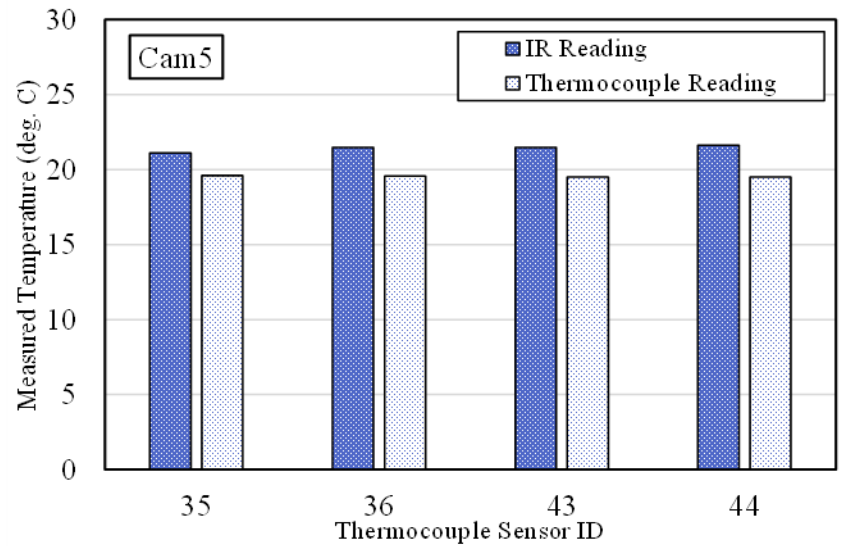
Table 1 Camera and Thermocouple information

Camera ID	No of Thermocouples	Thermocouple ID
Camera 1	6	7,8,9,16,17,18
Camera 2	5	4,5,6,14,15
Camera 3	5	20,21,22,27,28
Camera 4	5	26,33,34,40,41
Camera 5	4	35,36,43,44

To compare the offset between the thermocouple reading and the IR camera reading, thermocouple and IR temperatures at ambient conditions were compared. As the coordinate locations of the thermocouples and the camera field of views were already fixed, locating the exact IR reading was possible using the pixel information. To reduce the error associated with the data collection, a 3 ×3-pixel matrix was chosen, and the IR reading was averaged out from the 9 readings. The following images show the sample observed IR readings and the recorded thermocouple temperature at ambient conditions.







As the vane and camera location coordinates were properly documented, the temperature data from the body of the vane was removed and blanks were replaced with “NaN”. The edge of the vane was carefully drawn to avoid any loss of data. To properly collect the coordinate or the pixel values through which the vane edge passes an online semi-automatic intelligent image processing tool was used. The “WebPlotDigitizer” software and user instructions can be found here : <https://automeris.io/WebPlotDigitizer/userManual.pdf>

The similar process was performed for each of the camera images at each turbulence condition for both heated and adiabatic reading of temperatures. The cells filled with “NaN” were set to edit-restricted so that any issue with improper coordinate positioning would result to an error message from MS Excel. As the resolution of each image for the IR camera was set to 288×384 pixels, this was also checked for proper orientation of the image pixel values on the excel spreadsheet very precisely.

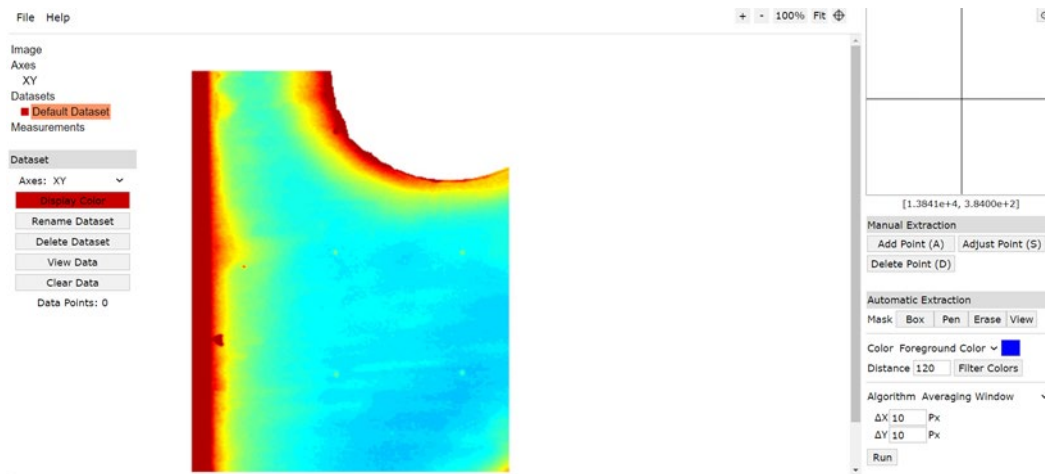


Figure 30 Web Interface and workspace of the “WebPlotDigitizer” GUI

After the Offset values were used to adjust the heated IR camera readings, an MS excel based worksheet was used to generate the Stanton Numbers for 15 different cases being studied. The calculated Stanton numbers were then further analyzed and processed using MATLAB software and image processing tool. Each of the camera images were collected separately to observe any discrepancy before masking. Finally, the masking and final production of the images were performed and further checked for any masking and overlapping issues.

CHAPTER IV

EXPERIMENTAL RESULTS

Experimental pressure measurements were acquired over the surface of the aft loaded vane and endwall. The measurements were taken at three different Reynolds numbers at low turbulence conditions. Three other pressure measurements were acquired, including an inlet pressure distribution, an exit pressure distribution, and a vane pressure distribution with static pressures obtained at the vane's mid-span. The heat transfer distributions were also taken at the surface of the endwall, reported in terms of Stanton number based on the cascade's exit conditions. This heat transfer distribution was measured both at the adiabatic and heated situations. These measurements help our understanding of the effects of secondary flows on the endwall heat transfer.

Uncertainty Analysis

The uncertainty analysis for this study was done using the root sum square method shown by Moffat [21]. These uncertainties emerge from many different sources of error, ranging from the data acquisition equipment, the fabrication of the parts, procedure, camera response, calibrator (blackbody), temperature accuracy etc. All uncertainties were calculated with a 95% confidence interval.

The uncertainty of the Stanton number, which is a derived value, was determined using perturbation analysis. The uncertainty in reporting the Stanton number for this study was calculated at a Reynolds number of 500,000 at the varying turbulence conditions to see if they

had any effect on the calculations. At the low Reynolds number and Stanton number condition, the radiation loss, which was the largest error source, was estimated to be 21 percent of the net surface heat flux. The radiative loss was slightly overestimated due to the view factor of the endwall surfaces to the heated vane. Because of this overestimation, the conduction loss was ignored. The Reynolds number was also estimated to have an uncertainty of 2 percent. There was uncertainty in the calculation in other areas such as the acquisition of the temperatures, both heated endwall temperatures and adiabatic reference temperatures, the measured voltage across the foil, the area of the foil, the emissivity of the foil, the measured density of the air, and the measured exit velocity of the air.

The recorded temperatures from the thermocouple sensor and IR camera were used to measure the difference of temperature reading or “Offset” (*Offset, $\Delta = \text{Thermocouple Temperature} - \text{IR camera temperature}$*). In the following figure, the individual differences, along with the average difference values, are shown. The positive difference indicates the measured thermocouple temperature was higher than the recorded IR camera temperature and vice versa. As the temperature of the thermocouple was considered more accurate, the offset values were added (when thermocouple > IR) or subtracted (when thermocouple < IR). The individual RMSE values are reported in the following Table and Figure. As the number of samples from each camera was not equal, thus the overall % error value was calculated by the weighted average of the number of available RMSE values from the “Observations” made for each camera. The overall RMSE value was calculated 13% for all the cameras together which is based on the absolute level of the local temperatures of infrared camera.

Table 2 Camera ID and Corresponding Estimated Offset

Camera ID	X	Y	No of Thermo	Obs1	Obs2	Obs3	Obs4	Obs5	Obs6	Diff= Thermo-IR	RMSE	Avg. Thermo Temp	%Error
Cam1	0	0	6	2.513	2.203	2.747	2.608	2.281	2.503	2.4759	2.7198	19.686	14%
Cam2	0	9.2	5	1.630	1.153	1.548	2.017	1.822	-	1.6342	1.8556	19.618	9%
Cam3	5.8	13.4	5	2.018	1.923	1.913	2.331	2.177	-	2.0724	2.324	19.562	12%
Cam4	8.65	22.6	5	2.965	3.354	2.832	2.405	3.303	-	2.9719	3.3451	19.524	17%
Cam5	12.4	14.45	4	-1.50	-1.91	-1.99	-2.11	-	-	-1.884	2.1914	19.541	11%

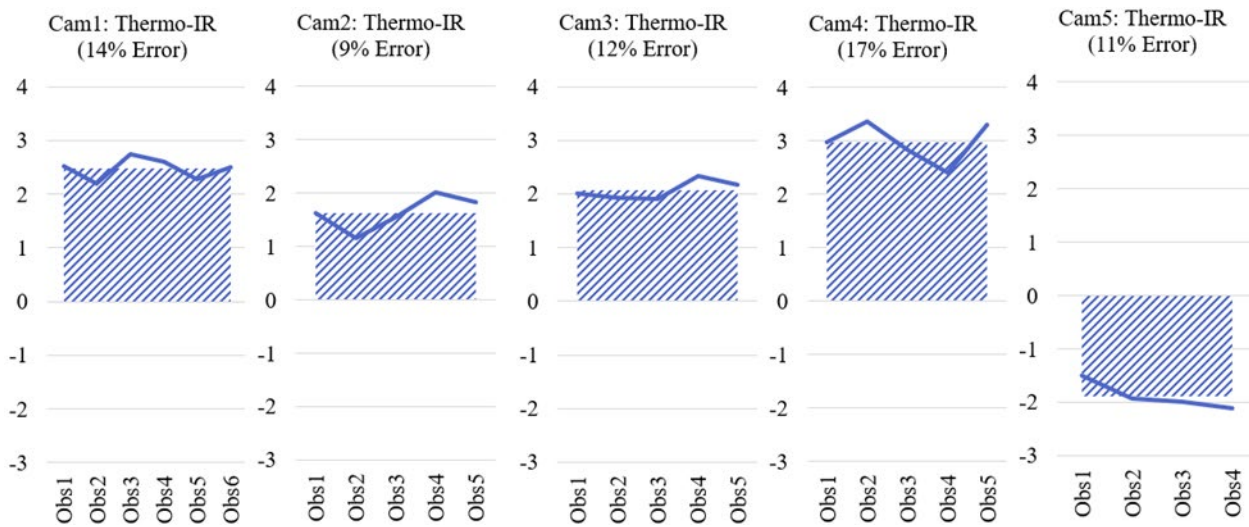
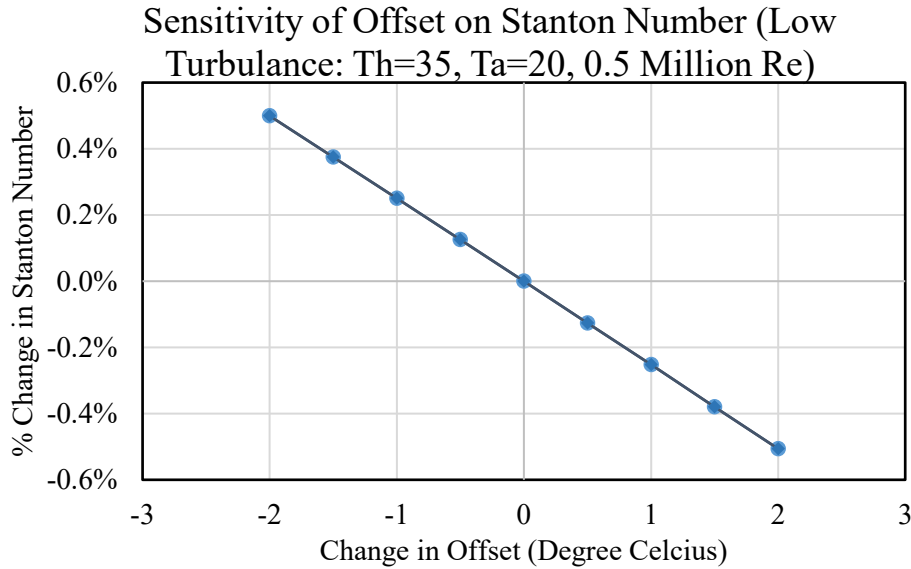


Figure 31 Estimation of the Offset for each Camera (camera 1 through camera 5)

To understand how the Offset value affect the Stanton Number, a trial imaginary heated temperature $T_h = 35^\circ\text{C}$, $T_a = 20^\circ\text{C}$, $Q'' = 391.041$, $V_{\text{exit}} = 15.66$ with a Reynolds Number = 0.5 M condition was chosen to experiment the sensitivity analysis. The following Figure indicate a maximum of 0.45% of the Stanton number is affected by the change of 2°C offset in the IR reading in heated condition.



To understand the uncertainty of the estimated Stanton numbers, the estimated Stanton number reading from the thermocouple and infrared camera were compared to estimate the error. The overall error from Stanton Number was recorded 7%, as shown in APPENDIX C.

Inlet and Exit Pressure Distributions

The inlet and exit pressure distributions were taken to determine the inlet uniformity and periodic nature of the exit flow through the cascade. These measurements boost our confidence in the produced aerodynamics quality of cascade. The inlet pressure measurements were obtained from 30 inlet pressure ports located one-quarter chord from the vane's leading edge plane. The inlet pressure distribution's periodic nature makes sense of the consistent spacing in both the x and y-directions for all vanes, as shown in Figure 32. The spacing on the x-axis is based on the pressure port's distance from the leading edge of the instrumented vane. A negative x value refers to the pressure port either placed in the first or second full passage of the cascade. A positive x value indicates that the pressure port is above the instrumented vane or in the third complete

entire passage. The y-axis is a pressure value. The plot, which is compared with that of Varty et al. [1], is shown in Figure 32.

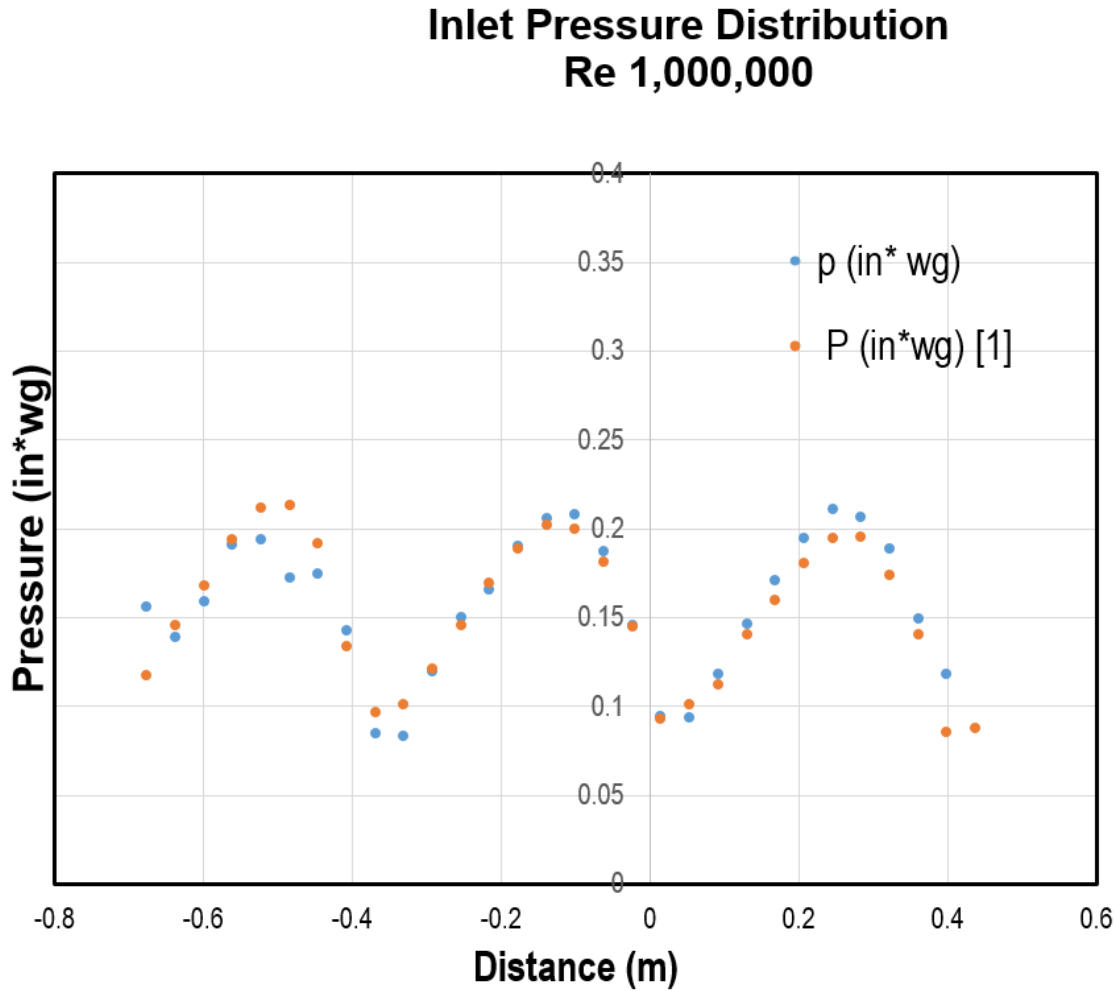


Figure 32 Low turbulence inlet pressure distribution Re 1,000,000

Likewise, 30 exit pressure ports were used for the exit pressure distribution, which helped us determine the periodicity of the exit flow. It also indicates the accurate placement of the vanes and the tailboards. The exit pressure distribution can be seen in Figure 33. The x-axis for this figure refers to the distance between the pressure port and the first pressure port, where the measurement starts from the bottom pressure port in the first passage. The y-axis is the pressure

value. Since the turbulence level's variation has little effect on the static pressure readings, both the inlet and exit distributions were exhibited at the low turbulence level. The exit pressure distribution is also compared with that of Varty et al. [1].

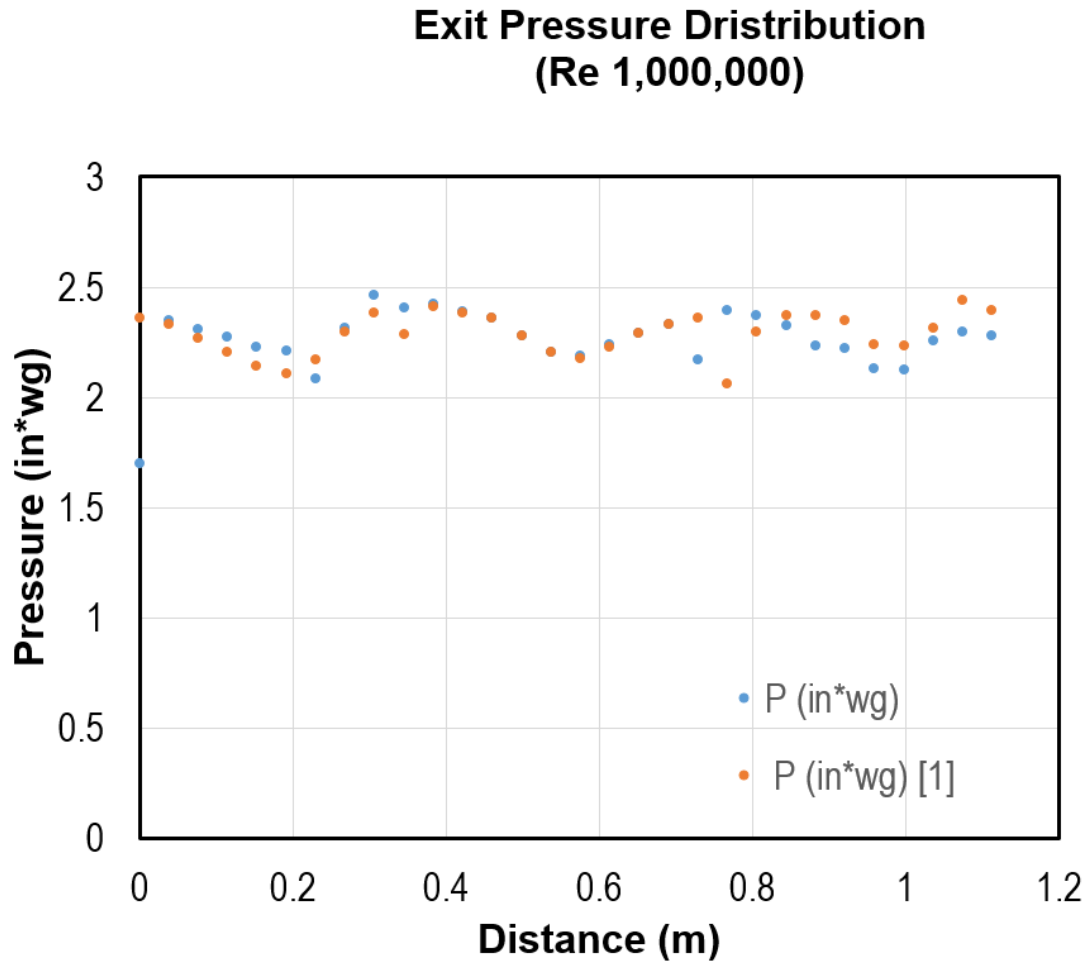


Figure 33 Low turbulence exit pressure distribution Re 1,000,000

Vane Pressure Distribution

The midspan vane pressure distribution is also crucial to check the aerodynamics quality of the baseline cascade. The pressure vane was developed with 40 static pressure taps located around the vane's surface with closer spacing around the leading edge of the vane. The instrumented

pressure vane was the third vane from the bottom. A midspan pressure measurement was acquired at all three Reynolds numbers, ranging from 500,000 to 2,000,000, for low turbulence levels. The turbulence level has less effect on the vane's pressure distributions, so only vane pressure distribution for low turbulence has been shown in

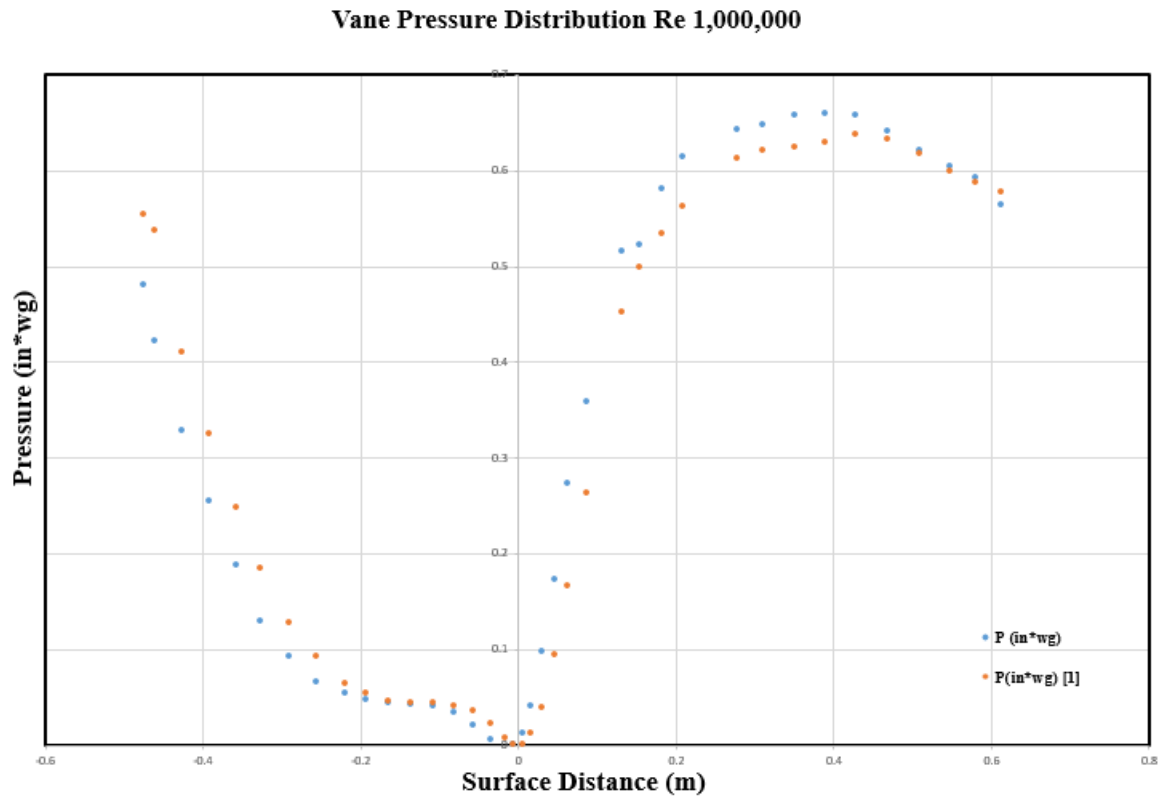


Figure 34. In Figure 34, the x-axis refers to the distance taken from the stagnation region (0 m), the negative distance representing the pressure surface, and a positive distance representing the suction surface. The plot has been shown in comparison with that of Varty et al. [1]. From Figure 29 to 31, each plot is in good agreement with the earlier measurement, which ensures the reliability of the baseline cascade's aerodynamics.

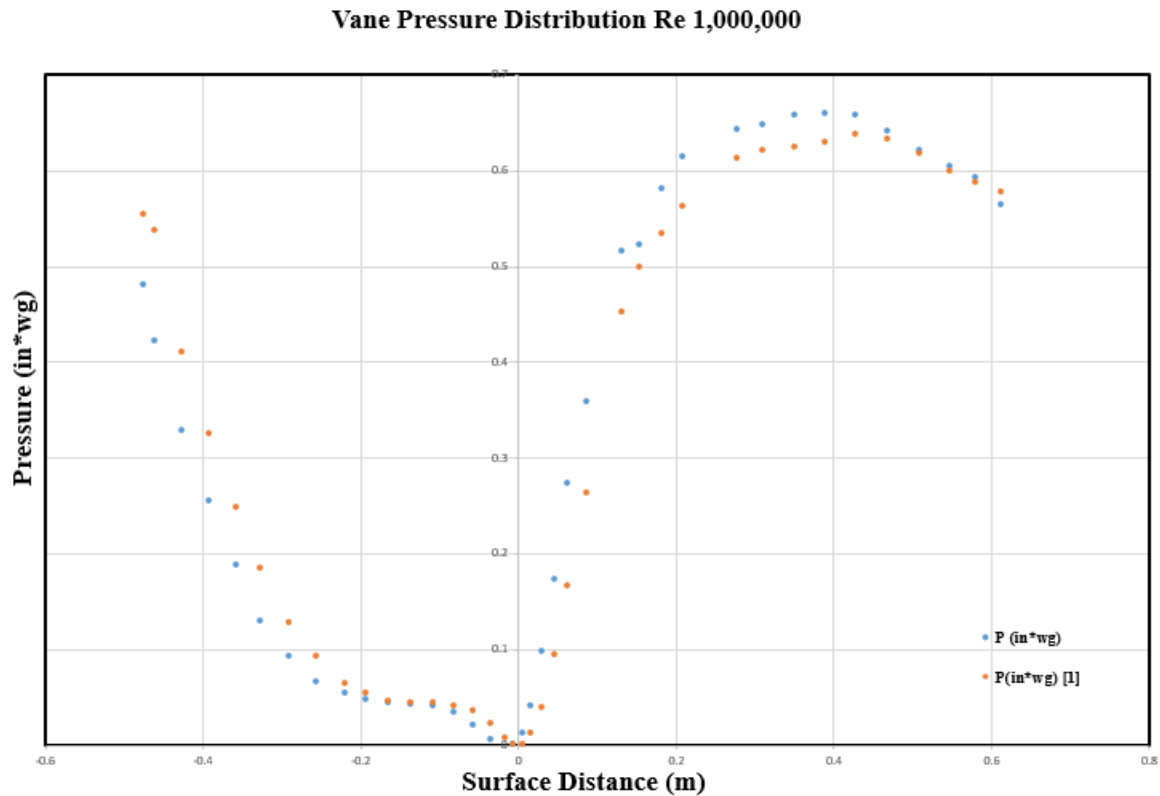


Figure 34 Low turbulence vane pressure distribution Re 1,000,000

Endwall Heat Transfer Measurements

Heat transfer measurements were taken for the endwall of the linear vane cascade and presented in the form of Stanton number distribution. The Stanton number distribution is calculated based on the exit condition of the cascade. In the process of documenting heated data, two endwall foils and the instrumented vane has been maintained constant heat flux while the upper and lower vane is unheated. The heater beneath the foils has been turned on to initiate constant heat flux condition and waited till the steady-state condition was achieved. The voltage across the foil and

the current through the foil have been printed out from the previously programmed quick basic software.

The surface heat flux was calculated from the recorded voltage and current of the foil per unit surface area.

$$Q = I \times V$$

$$Q'' = Q/A$$

The net surface heat flux is assumed to be the dissipated heat flux, excluding the radiation loss based on the local surface to adiabatic wall temperature. The emissivity (ϵ_m) used in this calculation was 0.95 since the endwall surface was painted in black. The heat transfer coefficient was calculated using the net surface heat flux divided by the temperature difference between the heated and unheated endwall surfaces. The difference between the two inlet temperature probes was considered during the measurement of net surface heat flux for better accuracy.

$$Q''_{net} = Q'' - \epsilon_m \times .0000000567((T_h + 273.15)^4 - (T_a + 273.15 + T_{Th} - T_{Ta})^4)$$

$$h = Q''_{net}/T_{diff}$$

$$T_{diff} = T_h - T_a + (T_{Th} - T_{Ta})$$

The heat transfer distribution of the endwall has been measured, and this heat transfer distribution is presented in terms of Stanton number based on the exit conditions.

$$St = h/(\rho \times V_{EXIT} \times C_p)$$

Endwall Stanton Number Distributions

In this thesis, the Stanton number visualization based on the equation mentioned above has been exhibited and discussed for five turbulence conditions varying three Reynolds numbers.

Figure 35. shows the Stanton number visualization for low turbulence conditions at half-million Reynolds number. The measured inlet flow for this condition exhibits the trait of the laminar boundary layer. Low turbulence conditions at low Reynolds number (.7%) experienced strong secondary flow phenomena. When the flow is heading towards the middle vane's leading-edge, the Stanton number level decreases as the thermal boundary layer thickens. But the endwall boundary layer separates while the flow approaching the stagnation region and forms a leading-edge vortex system known as the horseshoe vortex system. This horseshoe vortex formation region affects this region's heat transfer level and hence experiences the high heat transfer, as shown in the figure. One leg of the horseshoe vortex moves towards the vane's pressure side, and another leg moves towards the suction side of the adjacent passage due to the favorable static pressure gradient. The pressure leg separation line through the passage up to the adjacent vane's suction surface witnessed a low heat transfer level. There is a region where the separated streamlines from the horseshoe vortex's suction surface leg and the separated streamline due to the roll-up of the pressure surface leg of the horseshoe vortex by the passage vortex merges. This convergent region is consistent with the lowest heat transfer region on the endwall surface. The impact of these vortices convergence and their take-off onto the suction surface can be visible in

the Stanton number distribution along the suction surfaces of the upper and middle vanes. The turbulence developed at the trailing edge of the vanes from the trailing edge wake resulted in high heat transfer levels in the area downstream from the trailing edge. The high Stanton number in this region is curved in the circumferential direction, following the characteristic over turning near the endwall. The combination of endwall pressure gradients and low momentum fluid growth in the endwall region causes this overturning near the endwall. High heat transfer in the aft region of the surface is produced because of the corner vortices existence along the suction surface and the wake. The combination of high convective velocity and pressure gradient reduction of the pressure surface also attributed a relatively high Stanton number in the region downstream from that surface. Laminar or transitional flow is compatible with this Stanton number level. The heated vane presence does not appear to have a strong effect on this high heat transfer region. However, some significant differences are visible downstream from the trailing edges of the vane.

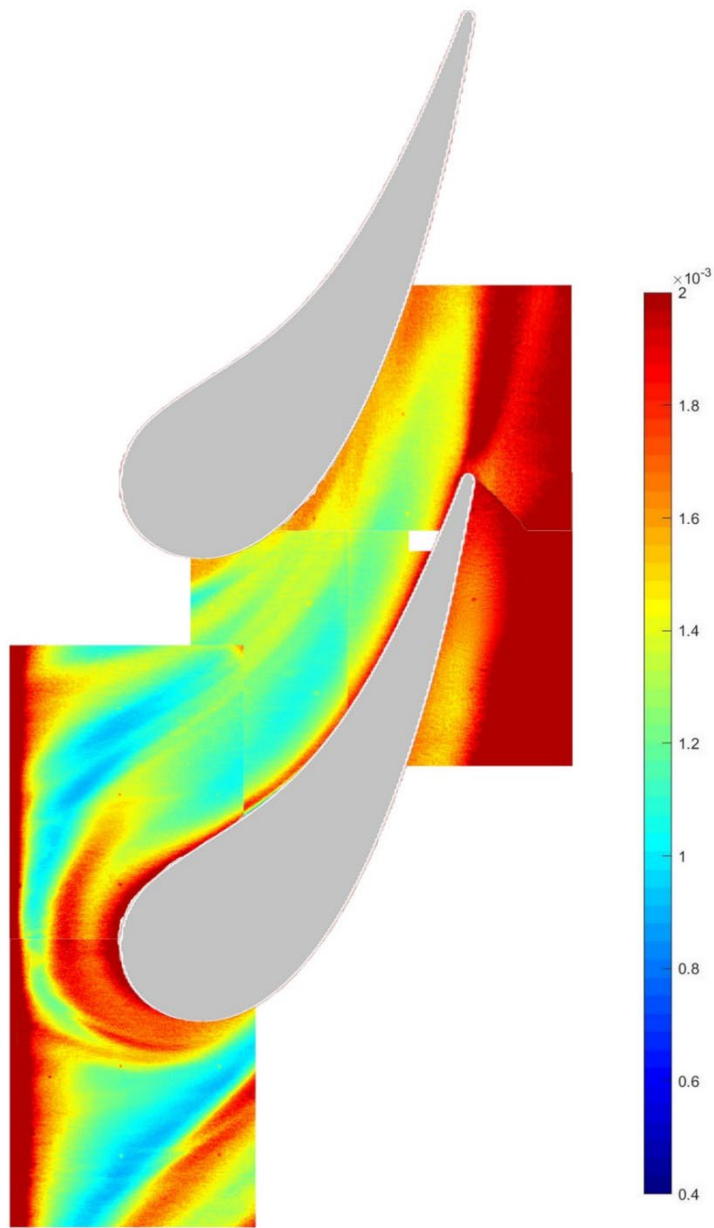


Figure 35 Endwall Stanton number distributions for low turbulence condition, $Tu = 0.007$, $Re_C = 500,000$

The Stanton number distributions for the small grid far generated turbulence at the 500,000 Reynolds number is shown in Figure 36. At this Reynolds number, the small grid far produces turbulence levels of around 3.5%. Elevated heat transfer levels were found around the stagnation region and downstream from the trailing edge like the earlier figure. It should be noted that the horseshoe vortex of two sides is dominant in the endwall flow field, and other vortices such as leading-edge corner vortex, suction surface corner vortex, passage vortex are present in the endwall surface. Passage vortex, a multi-vortex structure of the passage circulation, suction and pressure sides vortex, is also responsible for the heat transfer region of the endwall surface. The core of the suction and pressure side passage vortex near the endwall augmented the heat transfer level, which can be seen in the figure. The augmented heat transfer region in the passage is not as visible as the low turbulence one. These discrepancies can be attributed to the effect of the turbulence on the endwall separation. In this figure, the wake region downstream of the trailing edge is consistent with the high heat transfer level. The trend of the circumferentially directed curved heat transfer region is also visible here. High heat transfer in this region is present because of the combination of endwall pressure gradients and an accumulation of low momentum fluid in the endwall region. Additionally, high heat transfer in the aft region can be attributed to the existence of corner vortices along the suction surface and the wake.

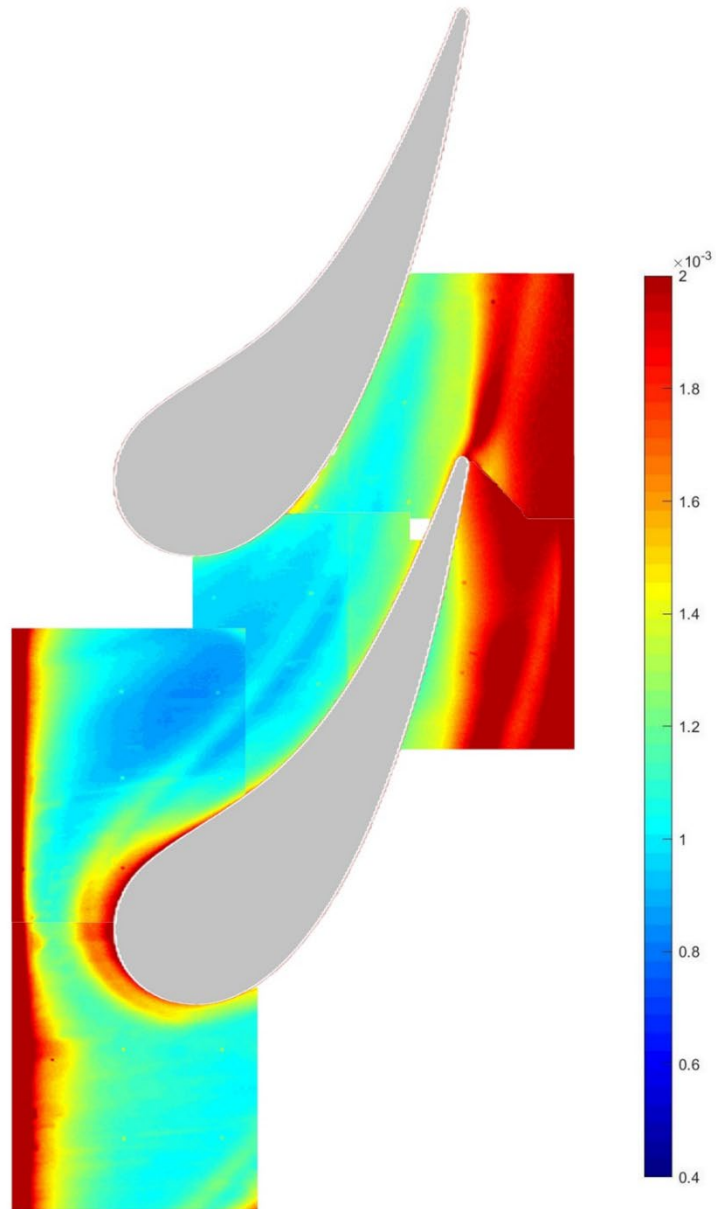


Figure 36 Endwall Stanton number distributions for small grid far turbulence condition, $Tu = 0.035$, $Re_c = 500,000$

Figure 37. shows the Stanton number distributions for the large grid turbulence case at the lowest Reynolds number. The measured turbulence for this case is around 8.1%. This case also shows a similar trend, like the other two turbulence cases. Suction and pressure sides of the horseshoe vortex enhance the heat transfer rate near the stagnation region. Passage circulation of suction side and pressure side forms as the inlet boundary layer rotates because of the large leading edge. For low turbulence, the core of this passage circulation is very close to the endwall. In this large grid condition from the figure, the comparatively high heat transfer region right is visible before the leading edge .This figure is also consistent with the low heat transfer region where the suction side horseshoe vortex and suction side passage vortex moves up the suction surface and away from the endwall. A very low heat transfer region in the middle of the pressure side and adjacent vane's suction side can be traced from the figure. Like that lower turbulence condition, the highest heat transfer levels are generally observed downstream from the vanes' trailing edge region due to the intense generation of turbulence, resulting in the wakes due to the velocity deficit.

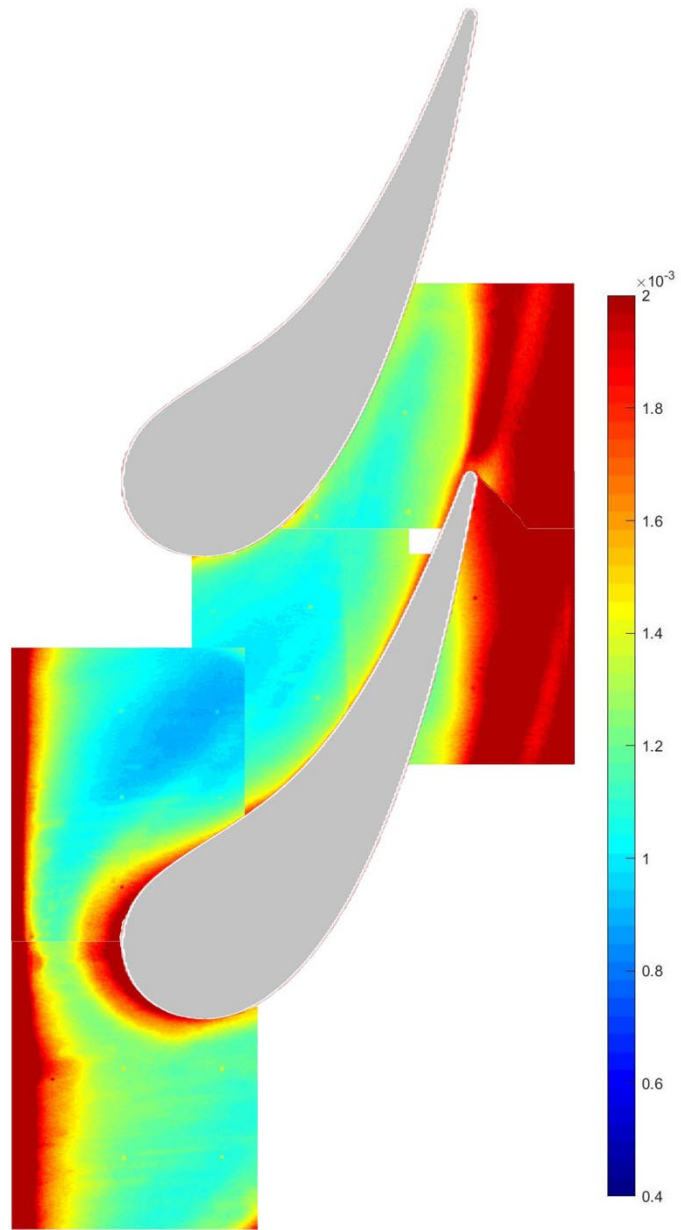


Figure 37 Endwall Stanton number distributions for large grid turbulence condition, $Tu = 0.081$,
 $Re_c = 500,000$

The Stanton number distributions for the mock aero-derivative generated turbulence at the 500,000 Reynolds number are presented in Figure 38. At this low Reynolds number, the mock aero-derivative combustor produces relatively high turbulence levels of around 13%. Similar to lower turbulence conditions, increased heat transfer levels were found around the stagnation region and downstream from the trailing edge. From the figure, it can be seen that the evidence of secondary flow becomes less apparent with the increasing turbulence condition. The large-scale turbulence can be accounted for these discrepancies. The presence of corner vortices along the suction surface affects heat transfer in the surface's aft region. From this figure, the high heat transfer region due to corner vortices is visible downstream of the surface. The highest heat transfer region is also found near the trailing edge due to the intense turbulence generation. Large scale turbulence effectively mixing away gradients in the flow in the normal, streamwise and lateral direction of the wall. This three-dimensional flow, especially the streamwise and lateral component flow, are actively moving around the flow structures. The turbulent movement effectively increases the heat transfer level by some percentage than that of lower turbulence cases. One thing has to be noted that even though the high heat transfer rate near the stagnation region is very clear from the figure, but the effect of the separation line is less apparent than that of the lowest turbulence condition.

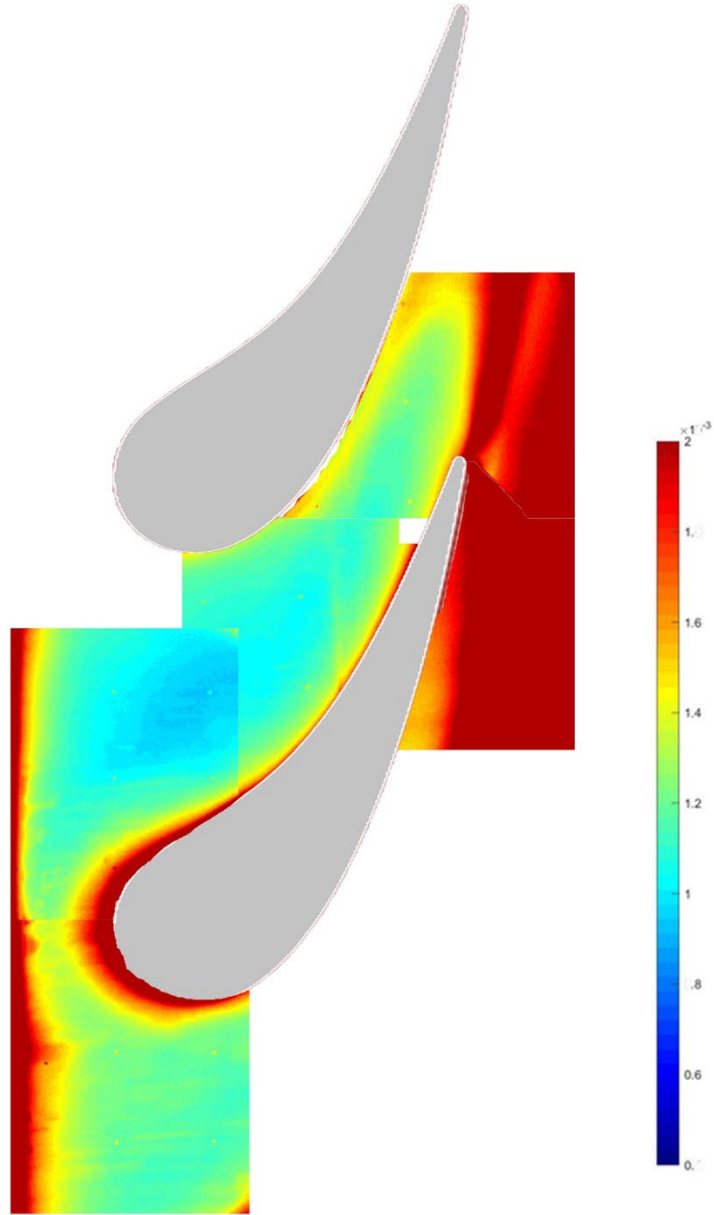


Figure 38 Endwall Stanton number distributions for aero derivative condition, $Tu = 0.137$, $Re_c = 500,000$

Figure 39. displays the Stanton number distribution for the high turbulence condition at a Reynolds number of 500,000. This high turbulence condition can generate a turbulence level of around 17.4%. Unlike the other low turbulence condition, the flow heading towards the vane's leading-edge exhibits a high heat transfer region because of the high turbulence. The interaction of unsteady flow structures due to turbulence makes the thermal boundary layer fuller. That's why the high heat transfer region can be seen even before the flow reaches the stagnation region consistent with the stagnation region. We didn't see that trend in earlier figures because the turbulence introduced in other cases is relatively small. A similar trend than that of the mock aero-derivative condition is present, including the pressure side toward the suction side and the high heat transfer region near the downstream and trailing edge of the endwall. The augmentation level of heat transfer is also higher in this case due to the mixing of turbulence

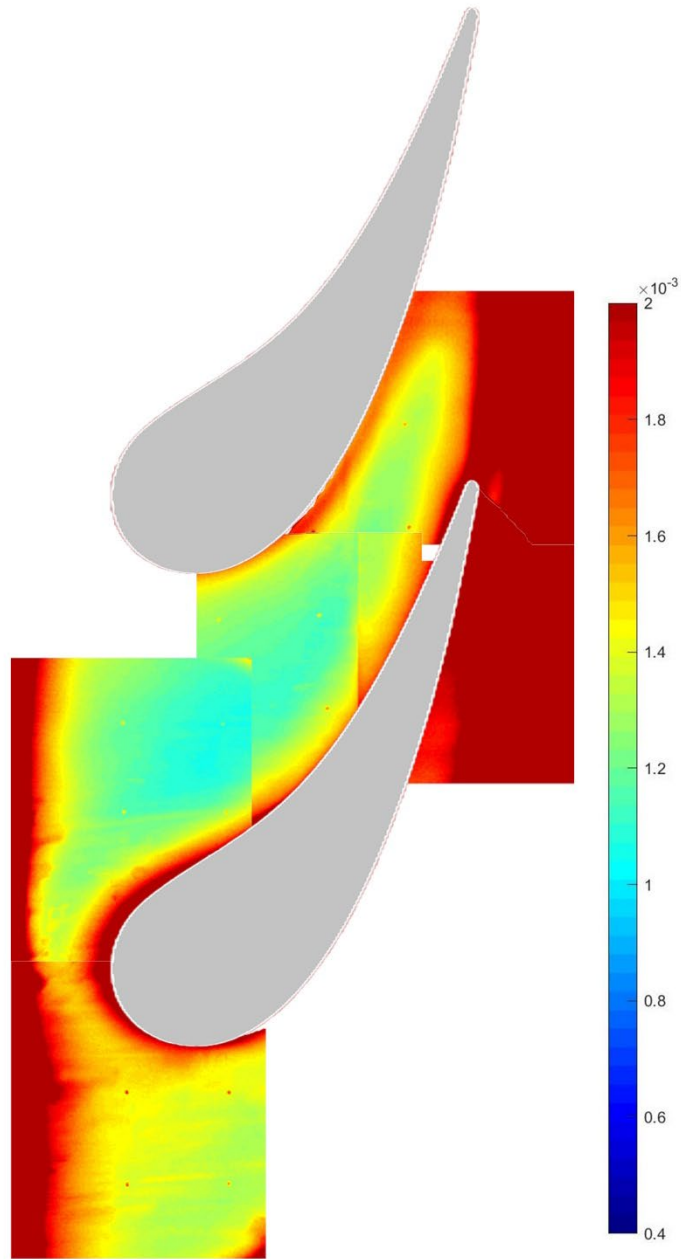


Figure 39 Endwall Stanton number distributions for high turbulence condition, $Tu = 0.174$, $Re_C = 500,000$

Figure 40 presents the Stanton number distribution for the 1,000,000 exit chord Reynolds number for the low free-stream turbulence case. The patterns show a similar trend to the 500,000 Reynolds number case for the low turbulence condition. The measured inlet flow represents a flow that is either laminar or just starting to transition. There are high Stanton number regions adjacent to the vane's leading-edge and above the pressure surface at the leading edge. There is a low Stanton number region below the suction surface at the leading edge. The presence of the pressure leg horseshoe vortex is visible just below the suction surfaces of the vanes. A high heat transfer region at mid arc along the suction surface due to the convergence is seen from the figure. There is a low Stanton number region adjacent to the mid arc on this figure's pressure surface. This low heat transfer region appears to be due to the downwash of laminar flow from the pressure surface. The wake at the trailing edge of the vane increases the heat transfer level. However, the high heat transfer region downstream of the middle vane's suction surface is visible from this figure. This high heat transfer region can be attributed to the highest velocities that occur just downstream from the trailing edge.

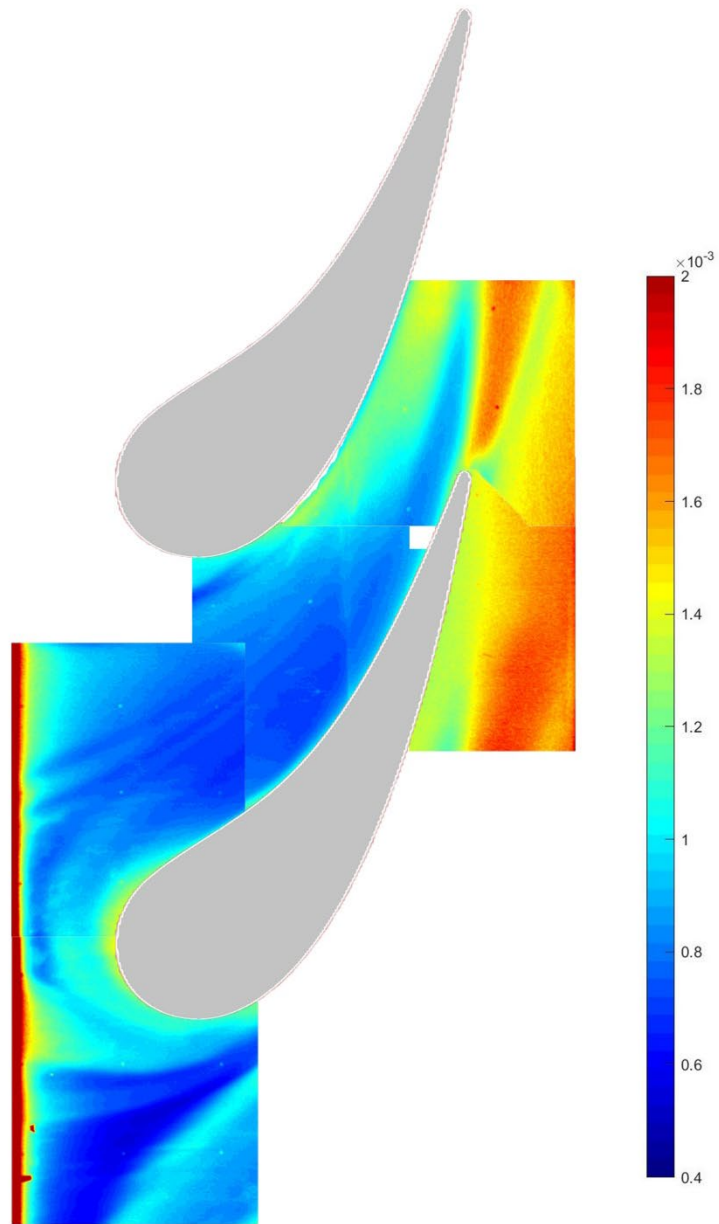


Figure 40 Endwall Stanton number distributions for low turbulence condition, $Tu = 0.007$, $Re_C = 1,000,000$

Figure 41 shows the endwall Stanton number distributions at a Reynolds number of 1,000,000 for the small grid far configuration's turbulence condition. This condition has a high turbulence intensity of 3.5 percent, and the exit flow produced by this turbulence generator may be considered either laminar or just starting to transition. The Stanton number distributions for this case are very similar to those seen for the low turbulence condition at the 500,000 Reynolds number, with the presence of secondary flows being especially evident. The highest heat transfer levels are once again can be traced in the leading edge region and the wake. There is also seen low heat transfer region due to the downwash of laminar flow from the pressure surface. This figure's heat transfer levels are slightly higher than those found in the low turbulence conditions at the same Reynolds number due to the more turbulence generation. Again, the leading edge and wake footprint are regions of high Stanton number distribution.

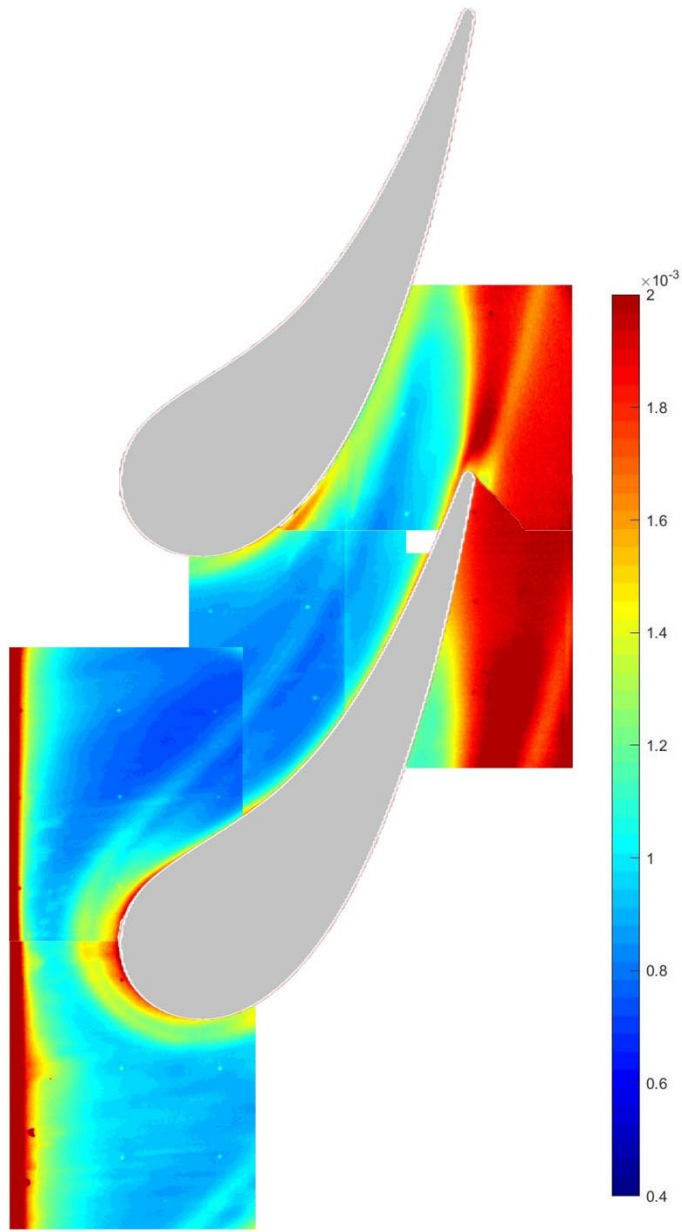


Figure 41 Endwall Stanton number distributions for small grid far turbulence condition, $Tu = 0.035$, $Re_c = 1,000,000$

The endwall Stanton number contours for the large grid turbulence condition at 1,000,000 Reynolds number are presented in Figure 42. This condition has a high turbulence intensity of 8.1 percent, and the exit flow produced by this turbulence generator may be considered either laminar or just starting to transition as well. The Stanton number flow patterns are very similar to those found in the lower Reynolds number., High turbulence cases in that turbulence seem smoother and do not show many correlations of typical secondary flow patterns. The highest heat transfer levels are once again apparent in the leading edge region and the wake. This figure's heat transfer levels follow the same level as those found in the same small grid turbulence conditions at the same Reynolds number. This similar heat transfer level is partly due to the thin boundary layers present in the large grid conditions.

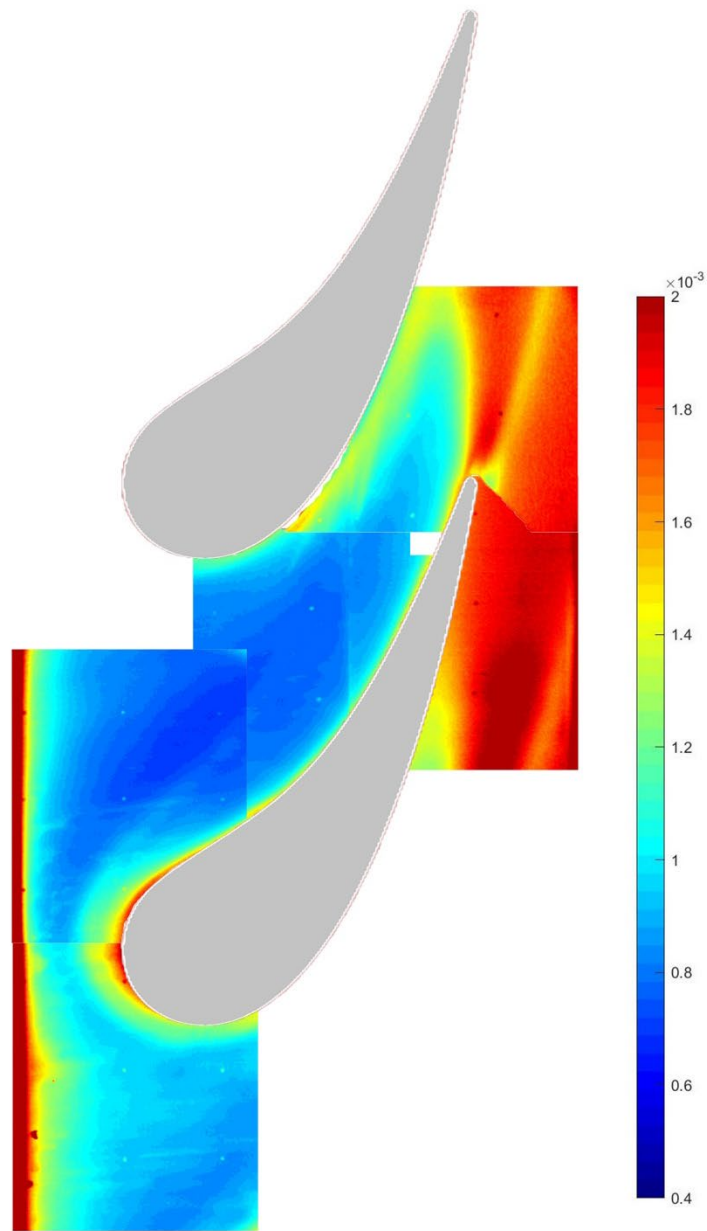


Figure 42 Endwall Stanton number distributions for large grid turbulence condition, $Tu = 0.081$,
 $Re_c = 1,000,000$

Figure 43 shows the endwall Stanton number distributions at a Reynolds number of 1,000,000 for the mock aero-derivative combustor's turbulence condition. This condition's turbulence intensity is as high as 13.7 percent, and the exit flow produced by this turbulence generator may be considered nonequilibrium channel flow. The Stanton number flow patterns are very similar to those found in the lower Reynolds number. However, similar to the lower Reynolds number comparison, the Stanton numbers pattern is smoother and has a weaker connection to typical secondary flow patterns. The highest heat transfer levels are once again found in the leading edge region and the wake. This figure's heat transfer levels are similar to those found in the low turbulence conditions at the same Reynolds number. There is also seen low heat transfer region due to the downwash of laminar flow from the pressure surface.

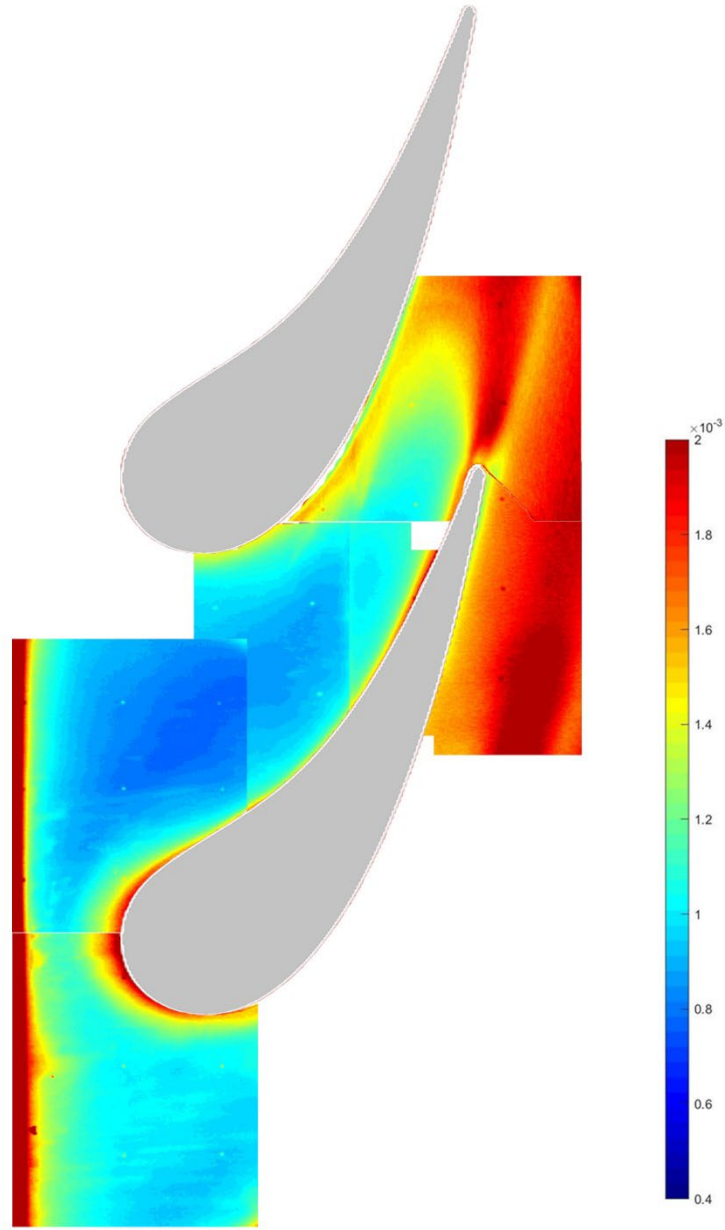


Figure 43 Endwall Stanton number distributions for aero-derivative turbulence condition, $Tu = 0.137$, $Re_c = 1,000,000$

Endwall Stanton number distribution taken at a Reynolds number of 1,000,000 is shown for the high turbulence condition in Figure 44. This condition produced turbulence levels around 17.4 percent. The encounter of high turbulence conditions enhances the flow structure's mixing and movement due to three-dimensional vortices. The Stanton number distributions are smooth and do not show any significant effects from the three dimensional vortices other than the elevated heat transfer levels adjacent to the leading edge. When the flow moves towards the leading edge, the suction side leg horseshoe vortex is apparent as it indicates a high heat transfer region. Another high heat transfer region in the area is downstream of the trailing edge. The overall Stanton number levels of this high turbulent case are relatively higher due to high turbulence

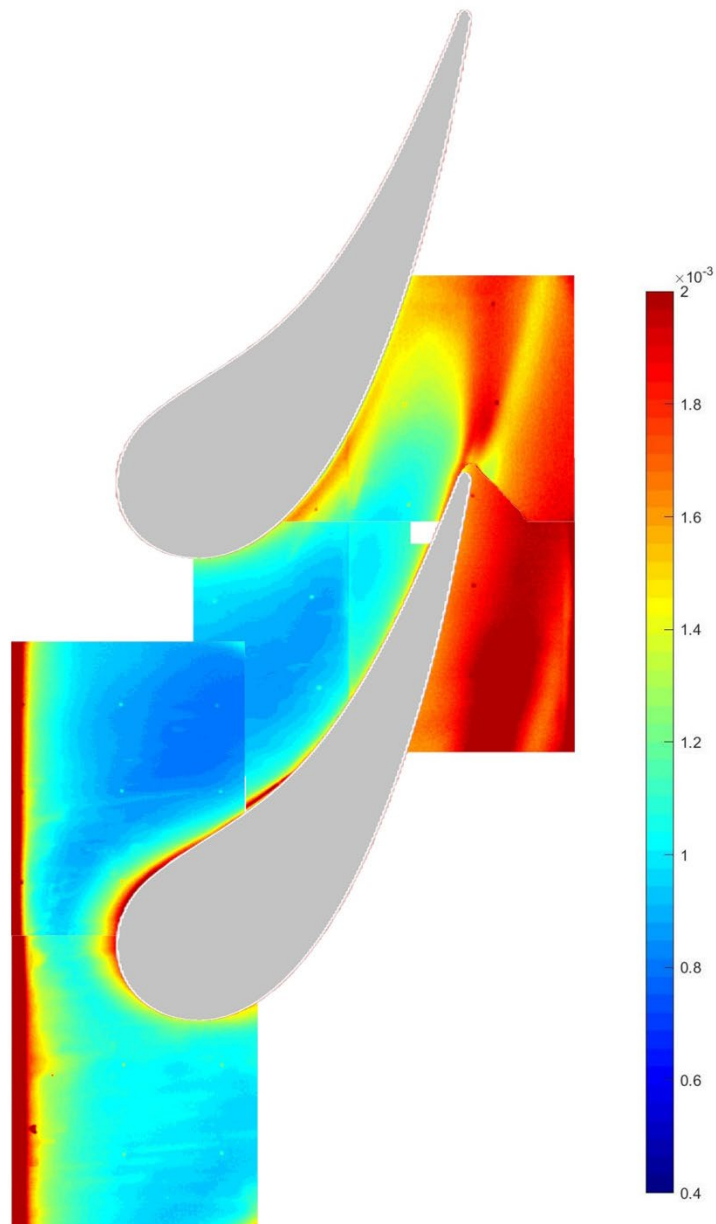


Figure 44 Endwall Stanton number distributions for high turbulence condition, $Tu = 0.174$, $Re_C = 1,000,000$

Figure 45 shows the endwall Stanton number distributions at the 2,000,000 exit chord Reynolds number for the low turbulence condition. The measured inlet conditions show turbulent boundary layers with low turbulent levels of around 0.7 percent. The secondary flow vortex system is still evident for this low turbulent condition. Patterns for this condition show a similar trend, including the vortex system's influence in the leading edge region, downstream from the trailing edge and off the suction surface where the two vortex systems merge and are swept off the endwall. The high heat transfer was evident at the pressure surface's trailing edge and in the wake region. A very low-heat transfer region just above the pressure surface is suggesting that the consistent thermal boundary condition, in this case, has a significant effect.

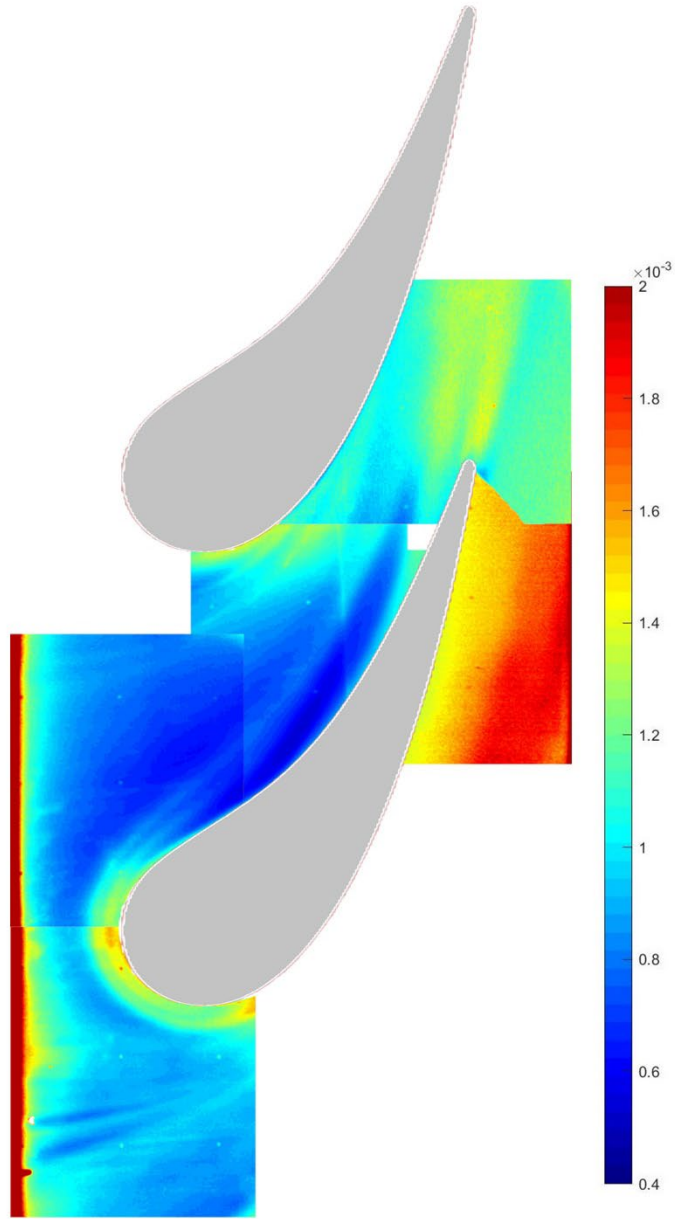


Figure 45 Endwall Stanton number distributions for low turbulence condition, $Tu = 0.007$, $Re_C = 2,000,000$

The Stanton number distribution for the small grid far turbulent condition at a Reynolds number of 2,000,000 is displayed in Figure 46. The measured inlet conditions show turbulent boundary layers with low turbulent levels of around 3.5 percent. The secondary flow vortex system is still apparent for this low turbulent condition. The low heat transfer region below the suction surface's leading-edge is noticeably present in this figure. The high heat transfer region is still visible along the suction surface in the region, the two vortex legs lift off the surface, in the passage from the pressure leg streamline, and in the region downstream the trailing edge. A very large low heat transfer region is traced just above the pressure surfaces of the middle vane. This low heat transfer region is caused by laminar fluid sweeping down off the pressure surface due to cross-passage pressure gradients. Two distinct high heat transfer areas downstream of the trailing edge are visible from the figure. One of these high heat transfer regions is generated by wake, and the other is likely generated by high velocities and thin turbulent boundary layers. Heat transfer is noticeably lower above the pressure surface in this figure, suggesting that the consistent thermal boundary condition case has a significant effect.

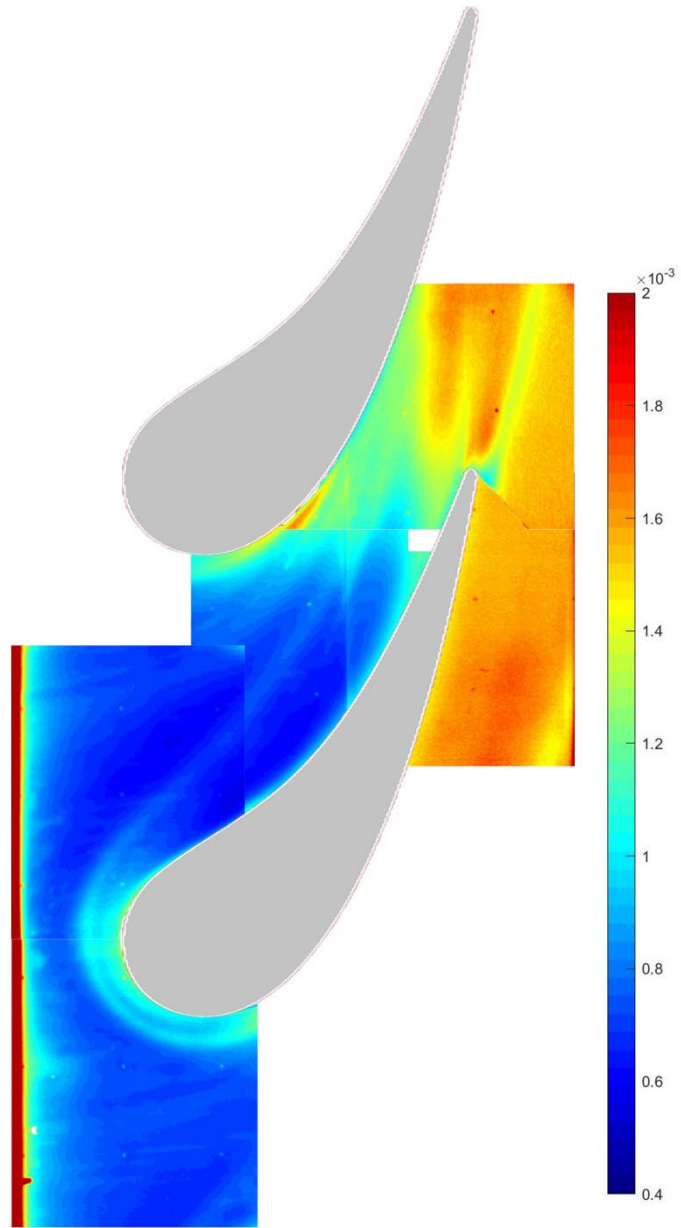


Figure 46 Endwall Stanton number distributions for small grid far turbulence condition, $Tu = 0.035$, $Re_c = 2,000,000$

The Stanton number distribution for the large grid turbulent condition at a Reynolds number of 2,000,000 is displayed in Figure 47. The measured inlet conditions represent turbulent boundary layers with turbulent levels of around 8.1 percent. This figure also follows a similar trend, including a high heat transfer region near the leading edge, downstream of the trailing edge and the wake region. However, the overall heat transfer level is lower than the other low turbulent condition at the same Reynolds number.

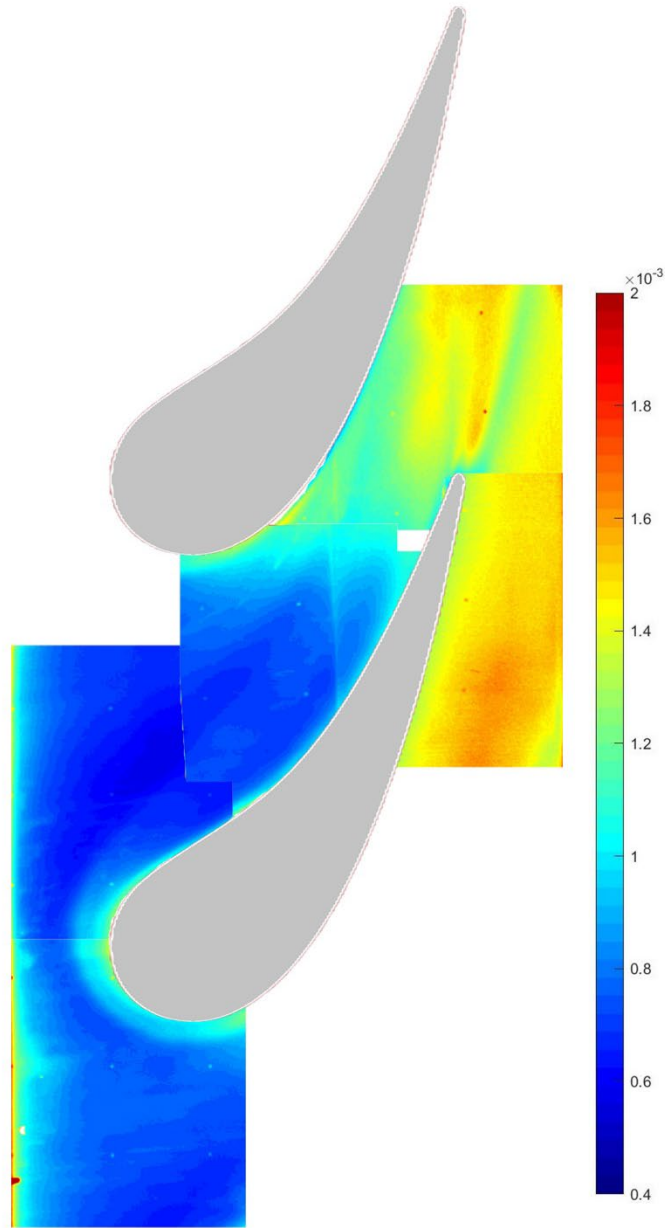


Figure 47 Endwall Stanton number distributions for large grid turbulence condition, $Tu = 0.081$,
 $Re_c = 2,000,000$

The Stanton number distribution for the high turbulent aero-derivative condition at a Reynolds's number of 2,000,000 is displayed in Figure 48. The aero-derivative combustor developed inlet airflow with peak velocities at mid-span and generated turbulence levels around 13.7 percent. Since a high turbulence level is generated, the Stanton number distributions are smooth and do not show much evidence of secondary flows. Again, the heat transfer level is similar to that of large grid turbulent conditions at the same Reynolds number.

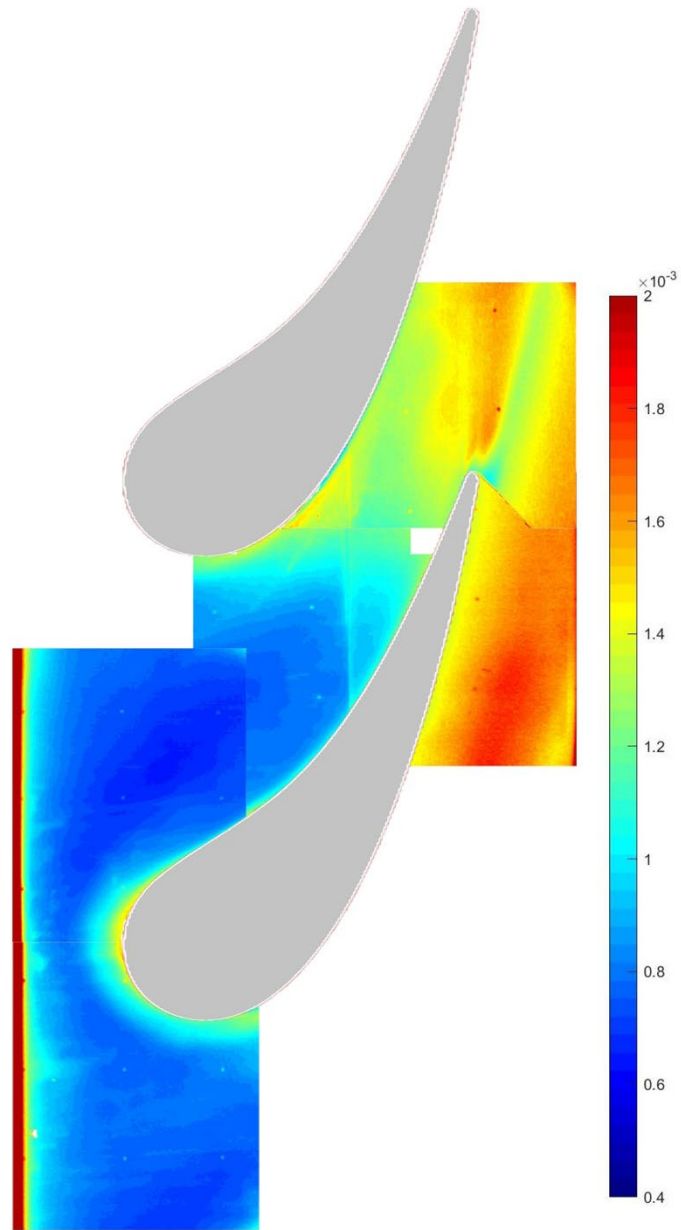


Figure 48 Endwall Stanton number distributions for aero-derivative turbulence condition, $Tu = 0.137$, $Re_c = 2,000,000$

Figure 49 shows the endwall Stanton number distributions for the high turbulent configuration at 2,000,000 Reynolds number. This configuration produces high inlet turbulence levels of around 17.4 %. The Stanton number distributions are smooth and show little evidence of the secondary flow. This turbulent condition also follows a similar trend of low and high heat transfer region. For example, a large low heat transfer region just off of the pressure surface due to laminar flow being swept onto the endwall surface can be traced in the figure. Also, there are two separate high heat transfer regions in the area downstream of the trailing edge shown from the figure.

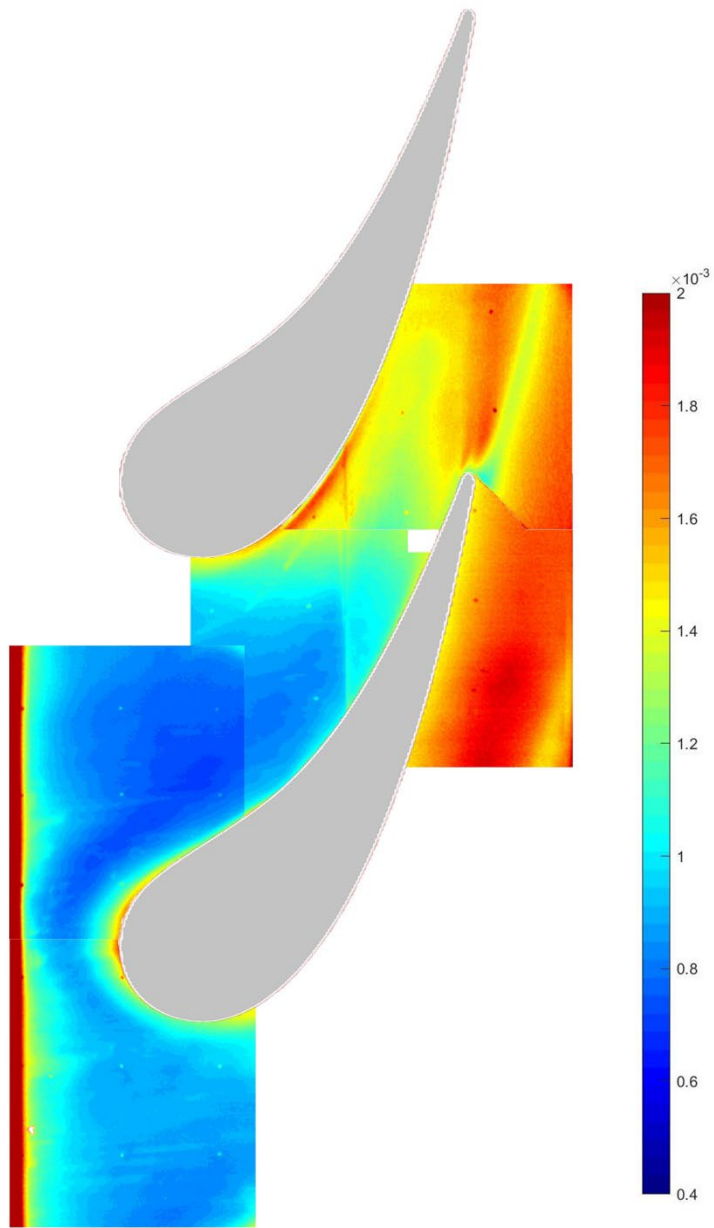


Figure 49 Endwall Stanton number distributions for high turbulence condition, $Tu = 0.174$, $Re_C=2,000,000$

CHAPTER V

CONCLUSION

The constant demand for more efficient and durable land-based gas turbines has opened the industry to explore many different designs. This experiment looked into more effective methods to cool and protect turbine components, especially the endwall of the first stage guide vane. Heat transfer measurements were acquired over the endwall surface at three different Reynolds numbers ranging from 500,000 to 2,000,000 and at five different turbulence conditions starting at 0.7% and going as high as 17.4%. The collected data are expected to be useful in the grounding of predictive methods for turbine endwall heat transfer, including the effects of turbulent augmentation and transition.

This thesis documents Stanton number distributions acquired in a linear turbine cascade, varying different turbulent conditions, whereas the in situ calibration has been considered for better accuracy. One of the Stanton number distribution has been documented at a low turbulence level and small grid far condition, which generates turbulence level up to 0.7% and 3.5%, respectively. One of the turbulent conditions was generated using a mock aero-derivative combustor that produces a turbulent level of 13.7 %. All configurations produce peak velocities at mid passage. Another configuration is representative of a large grid configuration and generates a turbulence level of 8.1%, whereas the other configuration produces high turbulence level of 17.4%. The low turbulence inlet condition was created using a contraction

nozzle among all turbulent conditions, producing relatively thin boundary layer. It is expected that the Stanton number visualization can provide insight as to the effects of Reynolds number and turbulence on endwall heat transfer.

The low turbulence heat transfer distributions produced by the nozzle, small grid and large grid show strong evidence of the influence of secondary flows on endwall heat transfer. The horseshoe vortex, passage vortex and trailing edge wake affected the heat transfer distribution on the endwall. This effect was apparent by the high levels of heat transfer seen near the leading edge, downstream from the wake, and in the passage at the trailing edge plane. Low heat transfer regions in the passage also provided evidence of the impact of secondary flows. The high-intensity large-scale turbulence enhances turbulent mixing and tends to push the vortex structures around on the surface. So for high turbulent conditions, a relatively weaker effect of secondary flow is visible. High heat transfer rates in the leading edge and wake regions are still present due to the influence of the horseshoe vortex and wake. The overall heat transfer level for the high turbulent condition is larger due to mixing.

The level of turbulence also seemed to affect the heat transfer downstream of the turbine vanes. All the conditions showed a high heat transfer region downstream of the trailing edge due to the vane wake. At the 1 million and 2 million Reynolds numbers, the low turbulence conditions produced two high heat transfer regions downstream from the vanes. The wake influences one region and the other region is due to the thin turbulent boundary layer in the passage's high-velocity region.

The changing Reynolds number appeared to have influence on the heat transfer level of all five turbulence conditions. Increasing the Reynolds number has not augmented the Stanton number levels within the vane passage. It is clear from the inlet, Stanton number levels decreased with increasing Reynolds number.

Overall, the heated constant heat flux boundary condition on the vane generally affects the heat transfer level in the passage and downstream in the wake region. However, the influence of the active vane surface was not shown to be drastic.

APPENDIX A

CASCADE DIMENSIONS

All of the units for the cascade dimensions are presented in inches.

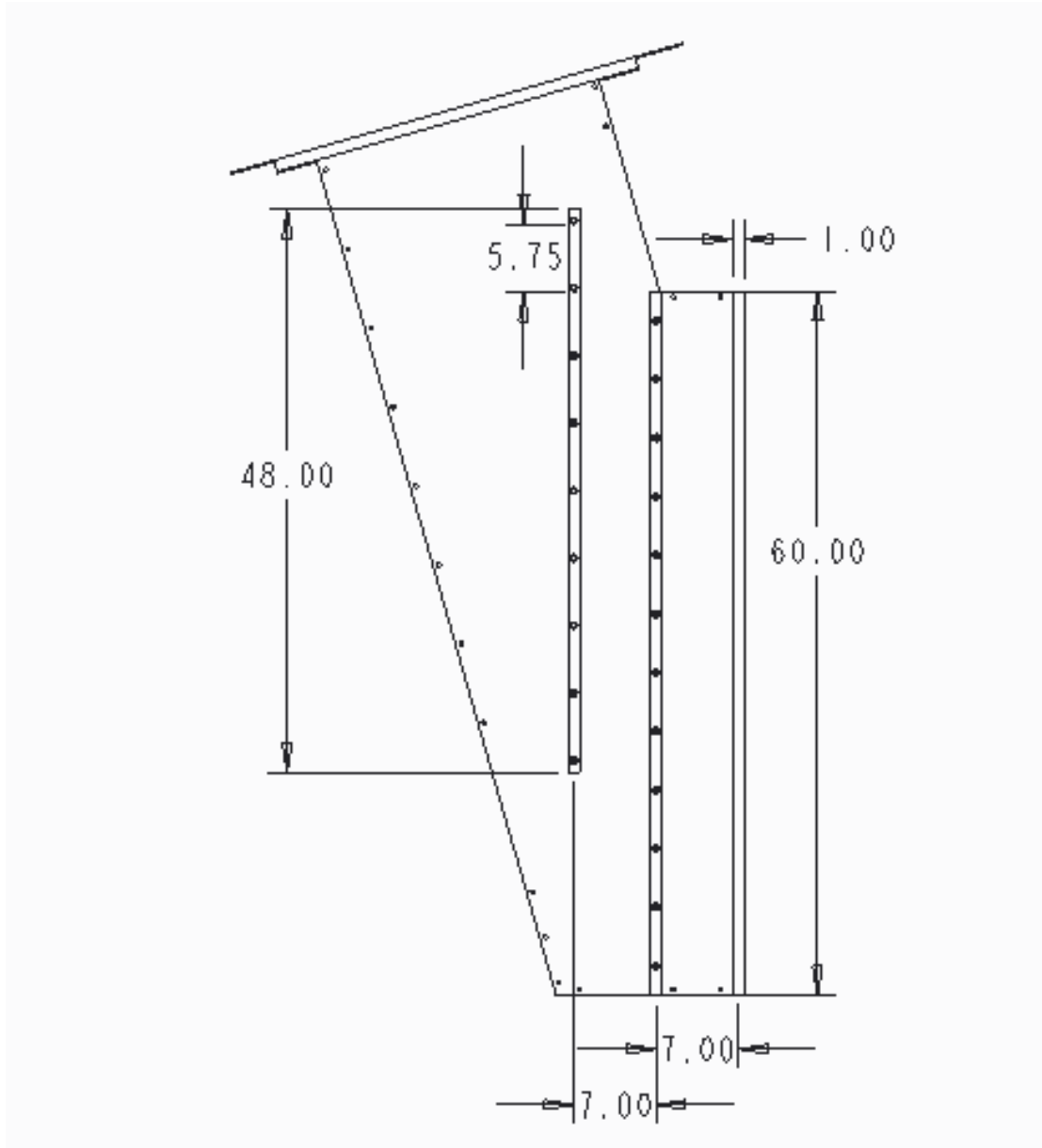


Figure 50 Cascade far endwall dimensions

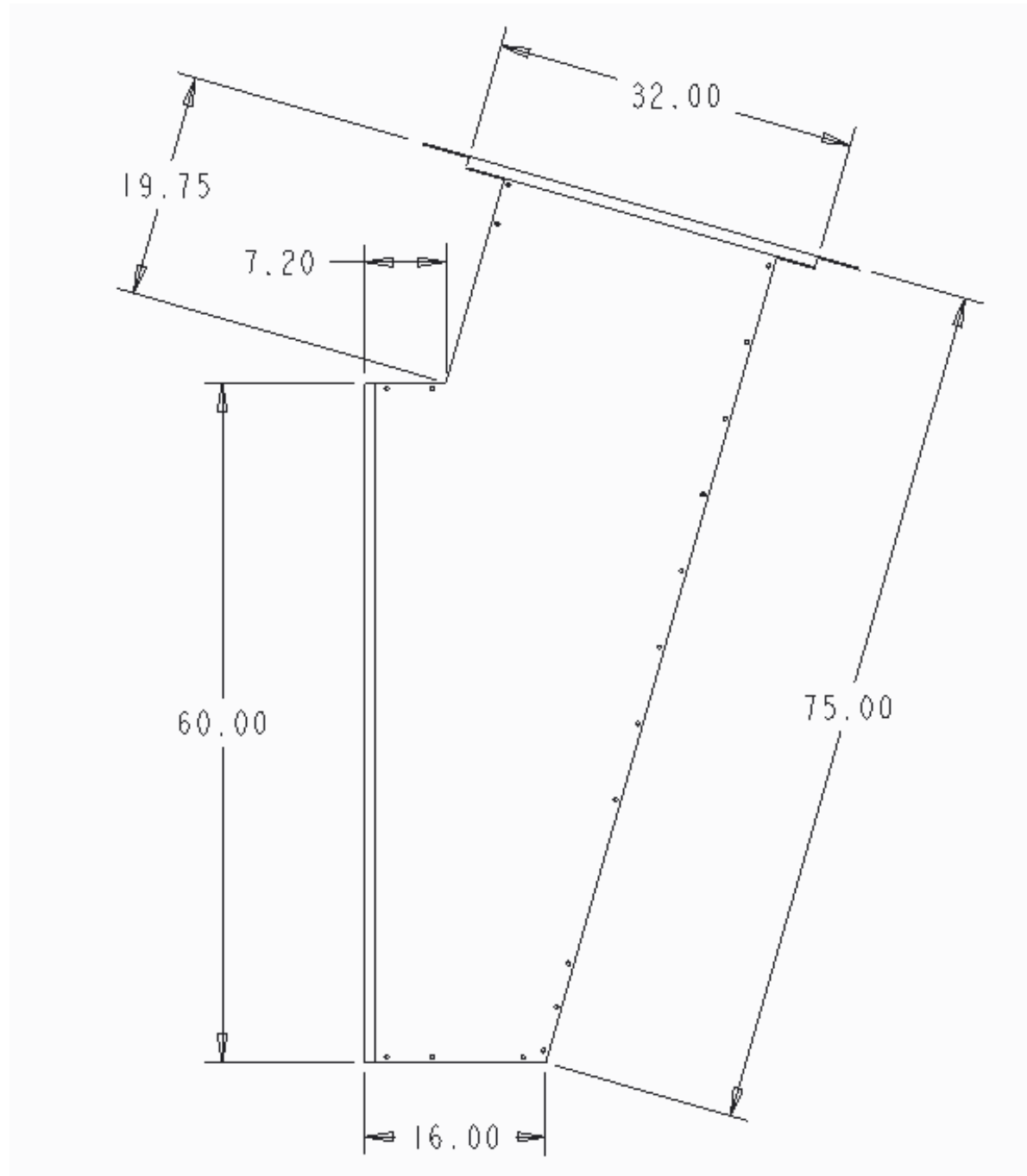


Figure 51 Cascade near endwall dimensions

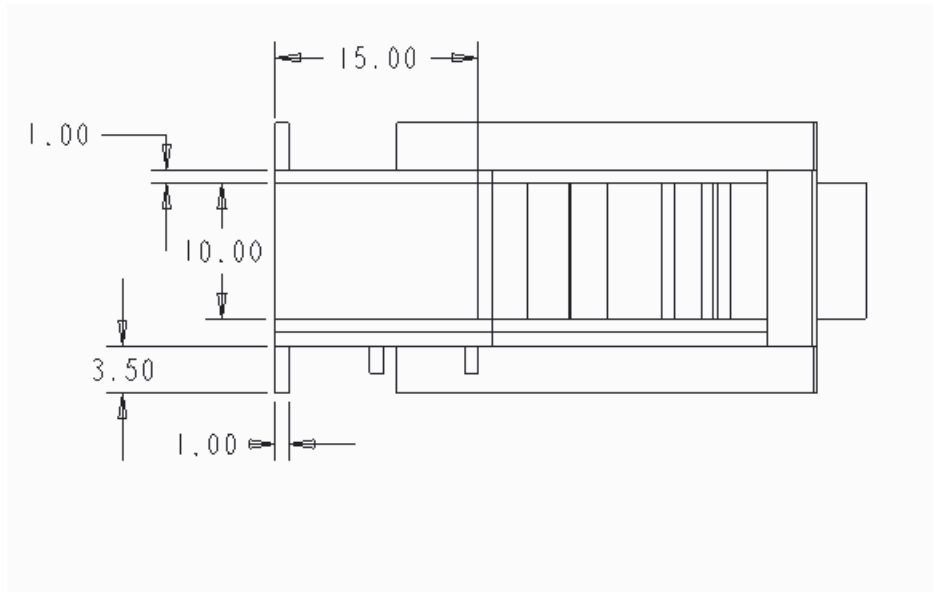


Figure 52 Cascade bottom dimensions

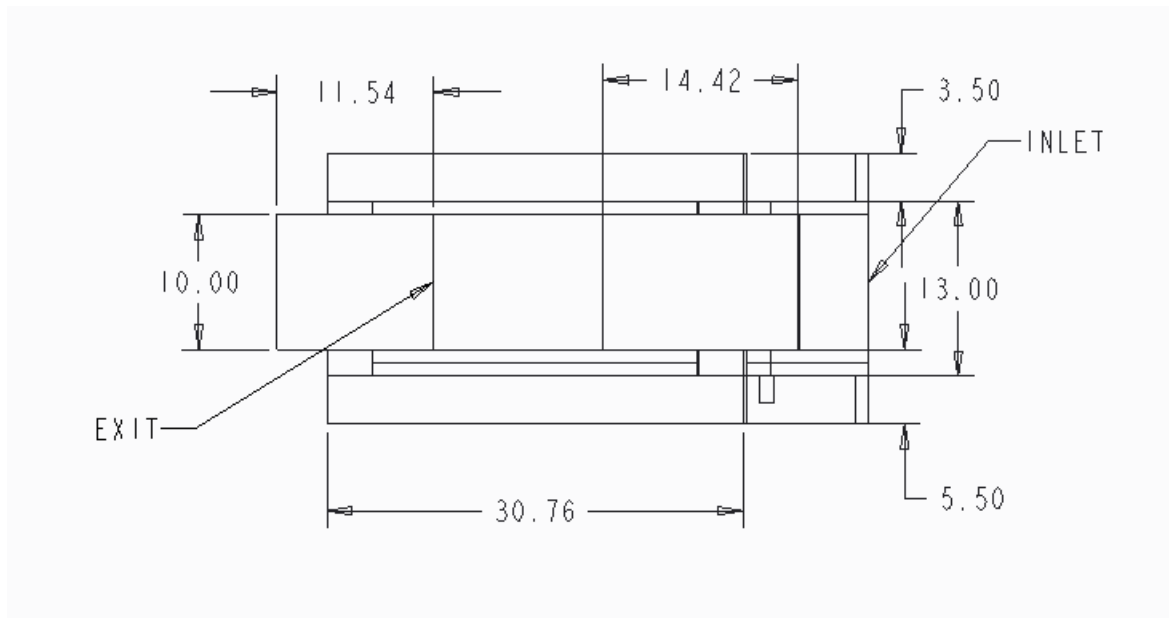


Figure 53 Cascade top dimensions

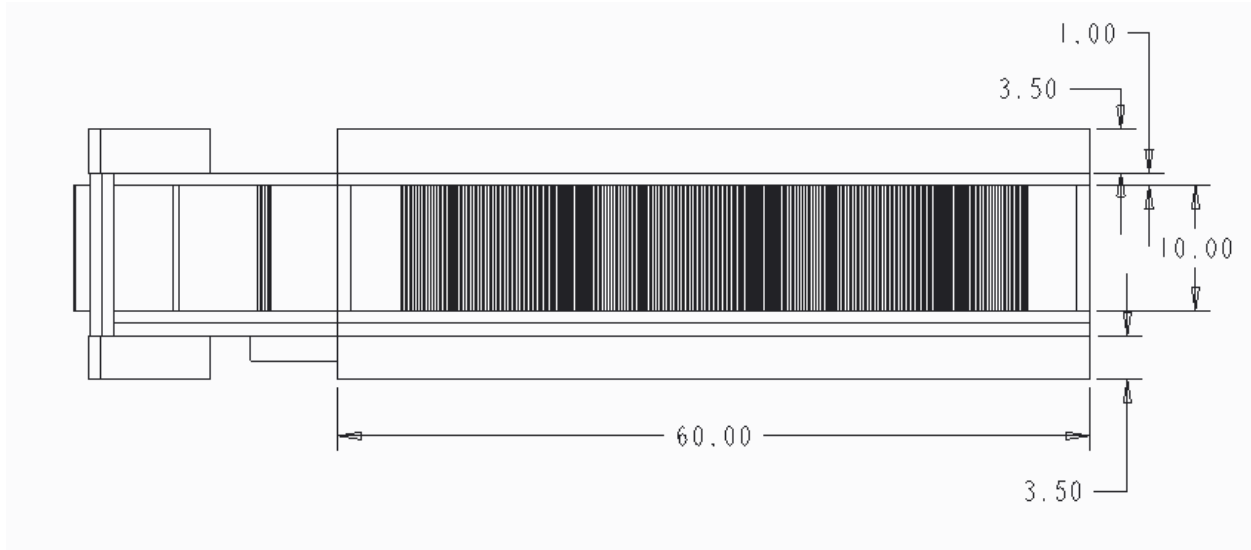


Figure 54 Cascade front dimensions

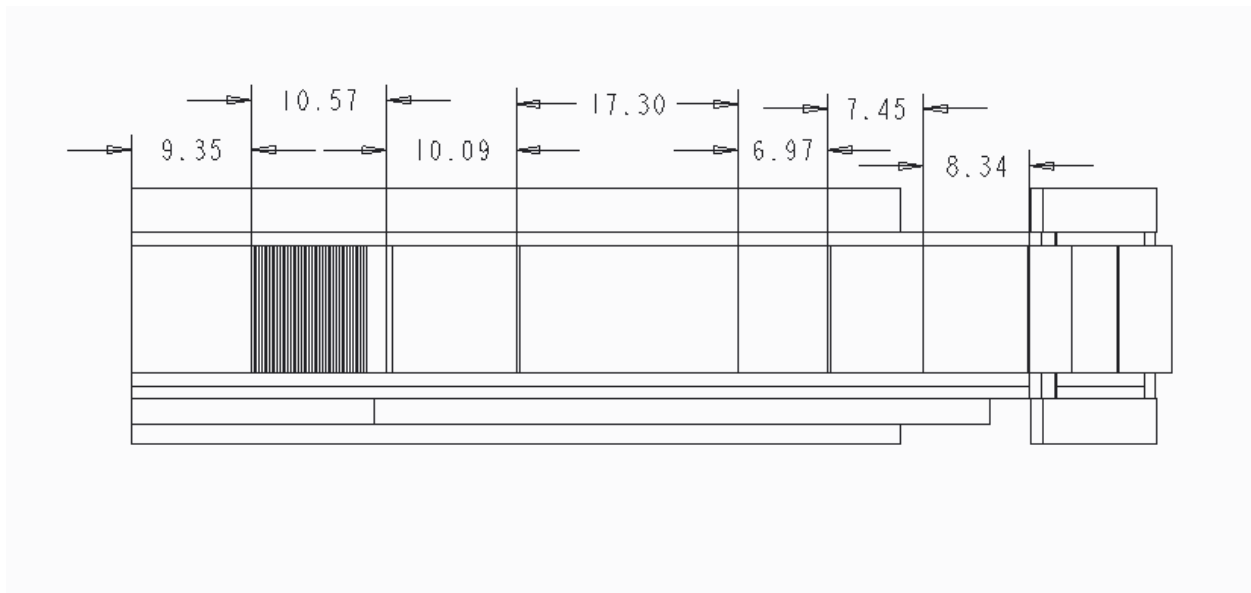


Figure 55 Cascade back dimensions

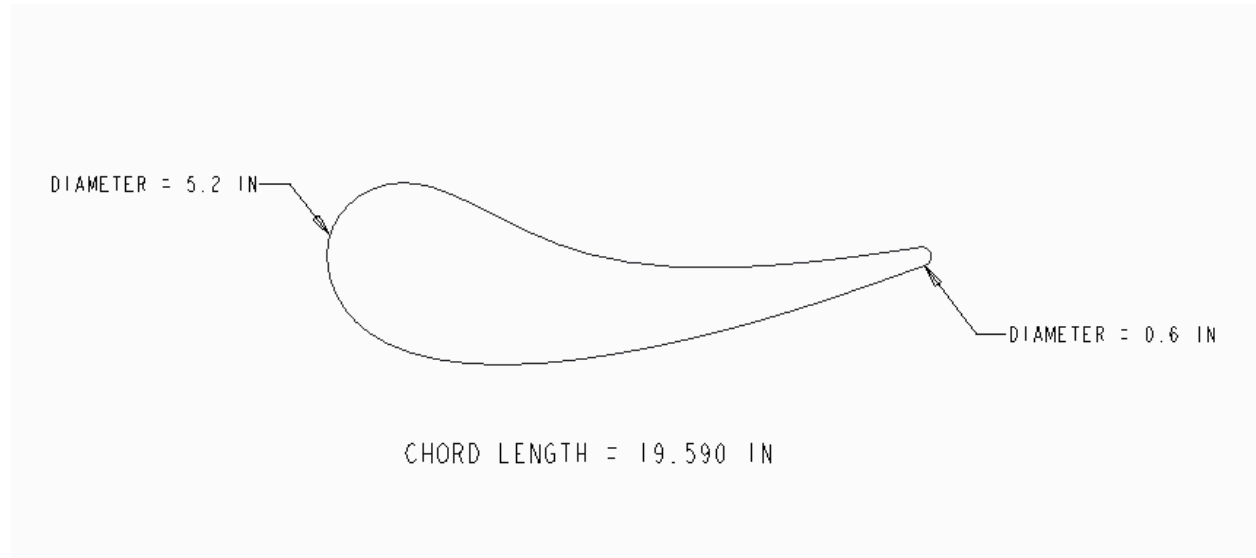


Figure 56 Vane dimensions

APPENDIX C

UNCERTAINTY ANALYSIS OF STANTON NUMBERS

ThermoLocation	Thermo St No	IR St No	Error%
7	0.000907	0.001124	24%
8	0.001028	0.001302	27%
9	0.000845	0.000975	15%
16	0.001116	0.000937	-16%
17	0.000642	0.000764	19%
18	0.001022	0.000967	-5%
4	0.000957	0.001023	7%
5	0.000702	0.000801	14%
6	0.000931	0.000962	3%
14	0.000827	0.00102	23%
15	0.000877	0.000983	12%
20	0.000939	0.001102	17%
21	0.000884	0.000997	13%
22	0.000746	0.000612	-18%
27	0.000773	0.000834	8%
28	0.000936	0.001249	33%
26	0.000941	0.001034	10%
33	0.000924	0.000758	-18%
34	0.000921	0.000861	-6%
40	0.001221	0.001489	22%
41	0.001291	0.000974	-25%
35	0.001051	0.000836	-20%
36	0.001083	0.001126	4%
43	0.001372	0.001584	15%
44	0.001387	0.001578	14%
		Average	7%

REFERENCES

- [1] Forrest E. Ames, Justin W. Varty, "Experimental Heat Transfer Distributions Over an Aft Loaded Vane With a Large Leading Edge at Very High Turbulence Levels," in *ASME 2016 International Mechanical Engineering Congress and Exposition*, Phoenix, Arizona, USA, February 8, 2017.
- [2] M. L. Nice, R. M. Hooper, L. S. Langston, "Three-Dimensional Flow Within a Turbine Cascade Passage," *Journal of Engineering for Power*, vol. 99, no. 1, pp. 21-28, January 1, 1977.
- [3] T. L. Butler, O. P. Sharma, "Predictions of Endwall Losses and Secondary Flows in Axial Flow Turbine Cascades," *The Journal of Turbomachinery*, vol. 109, no. 2, pp. 229-236, April 1, 1987.
- [4] Steven J. Olson, Richard J. Goldstein, Ernst R G. Eckert, Hai Ping. Wang, "Flow Visualization in a Linear Turbine Cascade of High Performance Turbine Blades," *J. Turbomach*, vol. 119, no. 1, pp. 1-8, 1997.
- [5] Ingram. G, Gregory-Smith, D. G., Harvey, N. W., "Investigation of a Novel Secondary Flow Feature in a Turbine Cascade With End Wall Profiling," *J. Turbomach.*, vol. 127, no. 1, pp. 209-214, 2005.
- [6] P. K. Dey, Forrest E. Ames, N. H. K. Chowdhury, "The Influence of Inlet Contraction on Vane Aerodynamic Losses and Secondary Flows With Variable Turbulence and Reynolds Number," in *Turbomachinery Technical Conference and Exposition*, Vancouver, British Columbia, Canada, 2011.
- [7] K. A. Thole, G. A. Zess, "Computational Design and Experimental Evaluation of Using a Leading Edge Fillet on a Gas Turbine Vane," *J. Turbomach.*, vol. 124, no. 2, pp. 167-175, 2002.
- [8] Mank. Sebastian, Duerrwachter. Lukas, Hilfer. Michael, Williams. Richard, Hogg. Simon, Ingram. Grant, "Secondary Flows and Fillet Radii in a Linear Turbine Cascade," in *Turbine Technical Conference and Exposition*, Düsseldorf, Germany, 2014.
- [9] T. J. Pralsner, E. Allen-Bradley, E. A. Grover, D. C. Knezevici, S. A. Sjolander, "Measurements of Secondary Losses in a Turbine Cascade With the Implementation of Nonaxisymmetric Endwall Contouring," *J. Turbomach*, vol. 132, no. 1, p. 132: 011013 , 2010.
- [10] R. E. York, L. D. Hylton, M. S. Mihelc, "An Experimental Investigation of Endwall Heat Transfer and Aerodynamics in a Linear Vane Cascade," *The Journal of Engineering for Gas Turbines and Power*, vol. 106, no. 1, pp. 159-167 , January 1, 1984.

- [11] P. W. Giel, D. R. Thurman, G. J. Van Fossen, S. A. Hippensteele, R. J. Boyle, "Endwall Heat Transfer Measurements in a Transonic Turbine Cascade," *The Journal of Turbomachinery*, vol. 120, no. 2, pp. 305-313, April 1, 1998.
- [12] R. J. Goldstein, R. A. Spores, "Turbulent Transport on the Endwall in the Region Between Adjacent Turbine Blades," *The Journal of Heat Transfer*, vol. 110, no. 4a, pp. 862-869, November 1988.
- [13] Forrest E. Ames, Pierre A. Barbot, Chao Wang, "Effects of Aeroderivative Combustor Turbulence on Endwall Heat Transfer Distributions Acquired in a Linear Vane Cascade," *The Journal of Turbomachinery*, vol. 125, no. 2, pp. 210-220, 2003.
- [14] A. Arisi, D. Mayo, Z. Li, W. F. Ng, H. K. Moon, L. Zhang, "An Experimental and Numerical Investigation of the Effect of Combustor-Nozzle Platform Misalignment on Endwall Heat Transfer at Transonic High Turbulence Conditions," in *Turbomachinery Technical Conference and Exposition*, Seoul, South Korea, 2016.
- [15] Zhigang Li, Luxuan Liu, Jun Li, Ridge A. Sibold, Wing F. Ng, Hongzhou Xu, Michael Fox, "Effects of Upstream Step Geometry on Axisymmetric Converging Vane Endwall Secondary Flow and Heat Transfer at Transonic Conditions," *The Journal of Turbomachinery*, vol. 140, no. 12, 2018.
- [16] T. W. Simon, J. D. Piggush, "Turbine Endwall Aerodynamics and Heat Transfer," *Journal of Propulsion and Power*, vol. 22, no. 2, 2006.
- [17] Alan. Thrift, Karen. Thole, Satoshi. Hada, "Impact of the Combustor-Turbine Interface Slot Orientation on the Durability of a Nozzle Guide Vane Endwall," *The Journal of Turbomachinery*, vol. 135, no. 4, p. 135(4): 041019, 2013.
- [18] G. Barigozzi, S. Ravelli, H. Abdeh, A. Perdichizzi, M. Henze, J. Krueckels, "Heat Transfer Analysis Over a Film Cooled Platform of a Vane Cascade With a Non-Uniform Inlet Flow," in *Turbomachinery Technical Conference and Exposition*, Charlotte, North Carolina, 2017.
- [19] Xing Yang, Zhansheng Liu, Qiang Zhao, Zhao Liu, Zhenping Feng, Fushui Guo, Liang Ding, "Measurements of detailed heat transfer characteristics on a high-pressure turbine vane endwall with coolant injection," *Experimental Thermal and Fluid Science*, vol. 109, 2019.
- [20] Borja. Rojoa, Carlos. Jimenezb, Valery. Chernorayc, "Experimental Heat Transfer Study of Endwall in a Linear Cascade with IR Thermography," in *EFM13 – Experimental Fluid Mechanics*, 2014.
- [21] R. J. Moffat, "Describing the uncertainties in experimental results," *Experimental Thermal and Fluid Science*, vol. 1, pp. 3-17., 1988.

